Why observed and modelled ozone production rates and sensitives differ, a case study at rural site in CHINA

Jun Zhou[1*#], Bin Jiang[1#], Bowen Zhong[1], Tao Zhang[2], Duohong Chen[2], Yuhong Zhai[2], Li Zhong[1], Zhijiong Huang[1], Junqing Luo[1], Minhui Deng[1], Mao Xiao[3,4], Jianhui Jiang[5,6], Jing Li[1], Min Shao[1*]

[1]College of Environment and Climate, Institute for Environment and Climate Research, Guangdong-Hongkong-Macau Joint Laboratory of Collaborative Innovation for Environmental Quality, Jinan University, Guangzhou 511443, China
[2]Environmental Key Laboratory of Regional Air Quality Monitoring, Ministry of Ecology and Environment, Guangdong Ecological and Environmental Monitoring Center, Guangzhou 511443, China
[3]Sichuan Academy of Environmental Sciences, Chengdu 610041, China
[4]Biogas Institute of Ministry of Agriculture and Rural Affairs, Chengdu 610041, China
[5]Global Institute for Urban and Regional Sustainability, School of Ecological and Environmental Sciences, East China Normal University, Shanghai 200241, China
[6]Institute of Eco-Chongming, East China Normal University, Shanghai 200241, China

[#] These authors contribute equally to this article

Correspondence to: Jun Zhou (junzhou@jnu.edu.cn) & Min Shao (mshao@jnu.edu.cn)

Abstract. Ground-level ozone (O_3) pollution has recently become of increasing concern in China. Studies have shown that conventional models often fail to predict accurately the net O_3 production rate ($P(O_3)_{net}$) due to the absence of certain mechanisms, particularly the kinetics from missing reactive volatile organic compounds (VOCs) species, and hence affects the reliability of evaluation for O_3 formation sensitivity (OFS). Therefore, we conducted a field observation of $P(O_3)_{net}$ and OFS using a $P(O_3)_{net}$ (NPOPR) detection system based on a dual-channel reaction chamber technique at the Guangdong Atmospheric Supersite of China in Heshan, Pearl River Delta (PRD) in autumn of 2023. The in-situ monitoring data were then compared with results from a zero-dimensional model incorporating the Master Chemical Mechanism (MCM v3.3.1). We tested the model performance by incorporating parameterization for 4 processes including HO_2 uptake by ambient aerosols, dry deposition, N_2O_5 uptake, and $ClNO_2$ photolysis, and found that the discrepancies between the modelled $P(O_3)_{net}$ ($P(O_3)_{net}$_Mod) and measured data ($P(O_3)_{net}$_Mea) did not change evidently, the maximum daily $P(O_3)_{net}$ differed by ~44.8 %. Meanwhile, we found that the agreement of OFS assessment results between the direct measurements and the modelling study was lower in the $P(O_3)_{net}$ rising phase (08:00-09:00, 63.6%) than in the $P(O_3)_{net}$ stable phase (10:00-12:00, 72.7%) and $P(O_3)_{net}$ declining phase (13:00-17:00, 72.7 %). The results in this study reflected that unmeasured oxygenated VOCs (OVOCs) were the most effective compensating factor for the discrepancies between observed and computed $P(O_3)_{net}$ and OFS, hinting clearly at the importance of quantitative understanding the total reactivity of VOCs in O_3 chemistry.

1 Introduction

Ground-level ozone (O_3) pollution has garnered widespread attention due to its adverse effects on human health (Chen et al., 2023), vegetation growth (Wang et al., 2017), and climate change (Li et al., 2016). Since the implementation of the *Air Pollution Prevention and Control Action Plan* by the State Council in 2013, particulate matter pollution in China has significantly decreased. However, ground-level O_3 pollution remains severe, and O_3 has become the primary pollutant affecting air quality in China (*China Environmental Status Bulletin*, 2013–2024). The variation in ground-level O_3 concentration is influenced by local photochemical production, surface deposition, and transport processes, which the following equation can express:

$$\frac{\partial[\mathrm{O_3}]}{\partial \mathrm{t}} = P(\mathrm{O_3})_{\mathrm{net}} - \frac{\mathrm{u_d}}{H}[\mathrm{O_3}] - \upsilon \cdot \nabla[\mathrm{O_3}] \tag{1}$$

In Equation (1), $\frac{\partial[\mathrm{O_3}]}{\partial \mathrm{t}}$ represents the change in O_3 concentration, $P(\mathrm{O_3})_{\mathrm{net}}$ denotes the net O_3 photochemical production rate, $\mathrm{u_d}$ is the O_3 deposition rate, H stands for the mixed layer height, and υ represents the wind speed. The in-situ photochemical production of ground-level O_3 primarily results from the photochemical reactions of precursors volatile organic compounds (VOCs) and nitrogen oxides (NO_X: NO+NO_2) under sunlight. The sensitivity of O_3 formation to its precursors is defined as the O_3 formation sensitivity (OFS), which can be classified into three regimes: NOx-limited, VOC-limited, or mixed sensitivity (Seinfeld & Pandis, 2016; Sillman, 1999). In an NOx-limited regime, the VOC/NOx ratio is high and O_3 production is controlled primarily by changes in NOx. In a VOC-limited regime, the VOC/NOx ratio is low, so O_3 decreases with additional NOx and increases with higher VOCs. In the mixed-sensitivity regime, O_3 rises when either NOx or VOC emissions increase (Wang et al., 2019). The $P(\mathrm{O_3})_{\mathrm{net}}$ is a critical indicator for evaluating local photochemical formation. The budget analysis of ground-level O_3 production ($P(\mathrm{O_3})$) and consumption ($D(\mathrm{O_3})$)can be calculated using the following equations:

$$P(\mathrm{O_3}) = \mathrm{k_{HO_2+NO}}[\mathrm{HO_2}][\mathrm{NO}] + \sum_i \mathrm{k_{RO_{2,i}+NO}}[\mathrm{RO_{2i}}][\mathrm{NO}]\varphi_i \tag{2}$$

$$\begin{aligned} D(\mathrm{O_3}) = {} & \mathrm{k_{O(^1D)+H_2O}}[\mathrm{O(^1D)}][\mathrm{H_2O}] + \mathrm{k_{OH+O_3}}[\mathrm{OH}][\mathrm{O_3}] + \mathrm{k_{HO_2+O_3}}[\mathrm{HO_2}][\mathrm{O_3}] \\ & + \sum_{\mathrm{i}} (\mathrm{k_{O_3+Alkene_i}}[\mathrm{O_3}][\mathrm{Alkene}_i]) + \mathrm{k_{OH+NO_2}}[\mathrm{OH}][\mathrm{NO_2}] + \mathrm{k_{RO_{2\mathit{i}}+NO_2}}[\mathrm{RO_{2\mathit{i}}}][\mathrm{NO_2}] \end{aligned} \tag{3}$$

$$P(\mathrm{O_3})_{\mathrm{net}} = P(\mathrm{O_3}) - D(\mathrm{O_3}) \tag{4}$$

Equations (2)–(4) illustrate the nonlinear dependence of the $P(\mathrm{O_3})_{\mathrm{net}}$ on the oxidation of precursors generating HO_X (=OH+HO_2) (Tong et al., 2025). Here, the $P(\mathrm{O_3})_{\mathrm{net}}$ is the difference between $P(\mathrm{O_3})$ and $D(\mathrm{O_3})$, k_{M+N} is the reaction rate constant between two molecules, φ_i represents the amount of NO_2 generated from the reaction of RO_{2i} with NO_2, and i denotes different RO_2 species. Currently, mainstream model simulation methods for calculating the $P(\mathrm{O_3})_{\mathrm{net}}$ primarily involve indirectly solving radical concentrations. However, existing models cannot fully characterize the complex radical cycling processes in the real atmosphere (Wei et al., 2023). Specifically, the incomplete mechanisms of RO_X (=OH+HO_2+RO_2) sources are particularly prominent, and these missing mechanisms affect the accuracy of RO_2 and HO_2 radical estimations to varying degrees. These include the neglect of contributions from carbonyl compounds, HONO, and OVOCs (Xu et al., 2022), as well as incomplete mechanisms for heterogeneous reactions on aerosol surfaces (Yang et al., 2022), dry deposition (Zhang et al., 2003), nitrosyl chloride photolysis (Whalley et al., 2021), and isomerization of isoprene peroxy radicals (Kanaya et al., 2012) remain inadequately understood. These gaps lead to systematic biases in the simulated $P(\mathrm{O_3})_{\mathrm{net}}$ (Woodward-Massey et al., 2023; Tan et al., 2017; Tan et al., 2019), thereby affecting the accurate determination of OFS.

It is noteworthy that there is a strong causal relationship between the aforementioned mechanistic biases and the misjudgment of OFS. Studies by Baier et al. (2017) and Tan et al. (2019) found that the observation-based model (OBM) significantly underestimates $P(O_3)_{net}$ under high NO_X conditions, leading to misjudgment of OFS. They pointed out that the unresolved VOC species and unspecified chemical mechanisms in the model are the primary causes of these biases. Similarly, Whalley et al. (2021) demonstrated that the zero-dimensional (box) model exhibits deviations in simulating $P(O_3)_{net}$ under high VOCs concentrations. Further research by Wang et al. (2024b) highlighted that the contribution of unidentified VOCs reactivity in anthropogenic emissions to O_3 formation is severely underestimated, and the missing VOC species and chemical mechanisms in existing models lead to biases in the determination of OFS. Such diagnostic biases in OFS may result in misjudgment of precursor emission reduction measures, thereby affecting the effectiveness of O_3 pollution control.

Direct measurement of $P(O_3)_{net}$ based on the dual-reaction chamber technique can address the aforementioned challenges. This concept was first proposed by Jeffries (1971), who suggested determining the real value of the $P(O_3)_{net}$ in ambient air by comparing the difference in $O_X(=O_3+NO_2)$ between a photochemical reaction chamber and a reference chamber. To date, several $P(O_3)_{net}$ detection systems based on the dual-reaction chamber technique have been developed, referred to as measurement of O_3 production sensor (MOPS), O_3 production rate measurement system (O3PR), O_3 production rates instrument (OPRs), net photochemical O_3 production rate detection system (NPOPR), Mea-OPR, or O_3 production rate-cavity ring-down spectroscopy system (OPR-CRDS) (Baier et al., 2015; Cazorla and Brune, 2009; Cazorla et al., 2012; Sadanaga et al., 2017; Sklaveniti et al., 2018; Hao et al., 2023; Wang Y. et al., 2024; Tong et al., 2025). Through practical applications in field observations, scholars generally agree that these detection systems offer rapid stability and high precision, with measurement uncertainties ranged from 10-30 %. Comparative studies have revealed that the underestimation of the simulated $P(O_3)_{net}$ can reach up to 50 % (Cazorla et al., 2012), highlighting the limitations of existing models in characterizing radical chemistry.

More importantly, the $P(O_3)_{net}$ detection system can diagnose OFS by quantifying changes in the measured $P(O_3)_{net}$ induced by different precursors through precursor addition experiments. Sklaveniti et al. (2018) first detected OFS in Indiana by adding NO to the sampling line of $P(O_3)_{net}$ detection systems, demonstrating the feasibility of directly measuring OFS with this device. Morino et al. (2023) combined a smog chamber with the $P(O_3)_{net}$ detection systems to directly measure OFS under baseline environmental conditions in Tokyo during summer. Chen et al. (2024) proposed the OPR_Adj parameter based on the $P(O_3)_{net}$ detection systems, which, through normalization of photolysis rates, diagnosed that O_3 photochemistry in Beijing is under VOCs control. These advancements indicate that the direct measurement method of OFS based on the $P(O_3)_{net}$ not only measures the actual OFS in ambient air but also quantifies the discrepancies between models and measurements.

In this study, we employed the developed NPOPR detection system based on the dual-reaction chamber technique to measure the $P(O_3)_{net}$ and OFS at the Guangdong Atmospheric Supersite of China in Heshan City, Pearl River Delta (PRD), in October 2023. Based on the observational data, we used the box model equipped with the Master Chemical Mechanism (MCM v3.3.1) to simulate the radical chemistry during the observation period. We compared and investigated the differences and influencing factors between the model-simulated values (abbreviated as $P(O_3)_{net_}$Mod) and the directly measured values (abbreviated as $P(O_3)_{net}$_Mea) in calculating the $P(O_3)_{net}$ and assessing OFS.

2 Methods and materials

2.1 Field measurements

Field observations were continuously conducted from 4–26 October 2023 at the Guangdong Atmospheric Supersite of China in Heshan City, located in northern Jiangmen, Guangdong Province (112.93°E, 22.73°N). The supersite is situated in the downwind area of Guangzhou, Foshan, and Dongguan, a region characterized by active secondary reactions and serving as a receptor for pollution transported from the industrial and urban centers (Luo et al., 2025; Huang et al., 2020). The surrounding area is primarily composed of farmland conservation zones and forested regions, with no major industrial sources. The supersite sits on a small mountain ~ 3 km from the nearest area heavy traffic corridor; at the observed mean wind speed of 2.8 m s^{-1}, the air mass from the corridor takes ~ 17 min to arrive. This separation limits spatial heterogeneity in both emissions and chemical composition, making the site well-suited for comprehensive monitoring and research on complex regional air pollution in the PRD (Mazaheri et al., 2019). The geographical location is shown in Fig. S1.

The $P(O_3)_{net}$ detection system (NPOPR), based on the dual-reaction chamber technique, was used to monitor the $P(O_3)_{net}$ and OFS. This system has been successfully applied in multiple field observation campaigns (Hao et al., 2023; Zhou et al., 2024a; 2024b). The detection system consists of a sampling unit, a monitoring unit, and a data acquisition unit. Ambient air passes through a Teflon particulate filter (7592-104, Whatman, UK) to remove particles larger than 2 μm before entering the dual chambers. The reaction chamber and the reference chamber are made of two identical quartz tubes (inner diameter: 190.5 mm, length: 700 mm, wall thickness: 5 mm). Unlike the reaction chamber, which allows ultraviolet light to penetrate and initiate photochemical reactions, the reference chamber is covered with an ultraviolet protective film (SH2CLAR, 3M, Japan) to block light with wavelengths below 390 nm, thereby preventing O_3 formation in the reference chamber. A custom circuit control system alternates the gas flow between the reaction chamber and the reference chamber into the NO reaction tube every 2 minutes, where the O_3 is converted to NO_2, which is then introduced into a Cavity Attenuated Phase Shift (CAPS)-NO_2 analyzer (Aerodyne Research, Inc., Billerica MA, USA). The gas not introduced into the NO reaction tube is expelled through an auxiliary pump. The data acquisition system detects NO_2, including both ambient NO_2 and NO_2 converted from O_3. By combining the average residence time (τ) of the gas in the chambers and the difference in O_X($\triangle O_X=\triangle(O_3+NO_2)$) between the two chambers, the $P(O_3)_{net}$_Mea can be calculated as Eq. (5):

$$P(O_3)_{net}\_Mea = P(O_X) = \frac{\Delta O_X}{\tau} = \frac{[O_X]_{reaction} - [O_X]_{reference}}{\tau} \tag{5}$$

The mean residence time in the reaction chamber is 0.15 h at the air flow rate of 2.1 L min^{-1}, and the limit of detection (LOD) of the NPOPR detection system is 0.86 ppbv h^{-1} at the sampling air flow rate of 2.1 L min^{-1}, which is obtained as three times the measurement error of $P(O_3)_{net}$ (Hao et al., 2023). The time resolution of the $P(O_3)_{net}$ measurement is 4 min. Our previous study demonstrated that $P(O_3)_{net}$ more directly reflects the photochemical O_3 formation potential from local precursors and is less affected by transport processes compared to O_3 concentrations (Zhou et al., 2024b). The measurement error of $P(O_3)_{net}$ is determined by the uncertainty in the Ox mixing ratio estimated for both the reaction and reference chambers. This uncertainty combines (i) the measurement uncertainty of the CAPS-NO_2 monitor used to derive Ox and (ii) the error induced by light-enhanced O_3 loss inside the chambers. Taken together, these contributions define the measurement precision of the NPOPR detection system. In addition, the measurement accuracy of the NPOPR detection system is 13.9 %, corresponding to the maximum systematic error arising from photochemical O_3 production in the reference chamber (Hao et al., 2023; Zhou et al., 2024b); details are given in Sect. S1 in the supplementary materials.

An additional system for the addition of NO or VOCs was added to the NPOPR sampling unit to assess OFS. The OFS was assessed by measuring the changes in $P(O_3)_{net}$ induced by the addition of NO or VOCs, enabling the direct measurement of OFS. A schematic diagram of the detection system is shown in Fig. S2. In the experiments for determining OFS through direct measurements (conducted daily from 8:00-18:00), each cycle lasted 1 hour. The first 20 minutes involved the addition of NO (denoted as $P(O_3)_{net}\_Mea^{+NO}$), the next 20 minutes measured the ambient baseline ($P(O_3)_{net}\_Mea$), and the final 20 minutes involved the addition of VOCs (denoted as $P(O_3)_{net}\_Mea^{+VOCs}$). Following Carter et al. (1995) and Wu et al. (2022), we select VOCs surrogates for the OFS measurement on the basis of ambient measurements previous to the measurements. From 4–11 October, the tracer mixture was formulated from the average daytime total VOC reactivity measured during 20 September–3 October 2023, and isopentane served as the alkane surrogate, ethylene and isoprene as the alkene surrogates, and toluene as the aromatic surrogate. For 13–26 October 2023, we used the average daytime total VOC reactivity obtained during 4–11 October 2023; ethylene represented non-methane hydrocarbons (NMHCs) and formaldehyde represented oxygenated VOCs (OVOCs). Each surrogate was mixed in proportion to its category's share of the ambient reactivity, and the effective precursor strength (NO or VOCs) should increase by 20 % relative to the original ambient level. For data treatment, we first interpolated $P(O_3)_{net}\_Mea^{+NO}$, $P(O_3)_{net}\_Mea$, and $P(O_3)_{net}\_Mea^{+VOCs}$ to 4-min resolution and then averaged them over 1 h to suppress data fluctuations. We caution that this 1-hour averaging may smooth out transient responses in the measured $P(O_3)_{net}$. The sensitivity of O_3 production to precursor changes was quantified using the measured OFS, derived from the incremental reactivity (IR) index. IR is defined as the change in $P(O_3)_{net}$ per unit change in precursor concentration ($\Delta S(X)$): a negative IR value indicates that reducing the precursor concentration increases O_3 production (e.g., decrease NOx would increase O_3 through OH mediate effect), while a larger absolute IR value suggests higher sensitivity of O_3 production to changes in the precursor. The IR was calculated as:

$$IR = \frac{P(\mathrm{O_3})_{\mathrm{net}}\_\mathrm{Mea}^{+X} - P(\mathrm{O_3})_{\mathrm{net}}\_\mathrm{Mea}}{\Delta S(X)} = \frac{\Delta P(\mathrm{O_3})_{\mathrm{net}}\_\mathrm{Mea}^{+X}}{\Delta S(X)} \tag{6}$$

where X represents VOCs or NO, $\Delta P(O_3)_{net}{}^{+X}$ represents the $P(O_3)_{net}$ values measured during the NO or VOCs addition period minus the $P(O_3)_{net}$ values measured when only injecting ambient air. $\Delta S(X)$ represents the concentration of the NO or VOCs precursor changed during the corresponding measurement period. We define the transition regime as the region over which the IR shows a simultaneous increase or decrease upon addition of both VOCs and NO.

In addition to $P(O_3)_{net}$ and OFS, hourly data such as $PM_{2.5}$, O_3, NO, NO_2, SO_2, carbon monoxide (CO), photolysis rates (j_{O^1D}, j_{NO_2}, $j_{H_2O_2}$, $j_{NO_3\_M}$, $j_{NO_3\_R}$, j_{HONO}, j_{HCHO_M}, j_{HCHO_R}), HONO, and VOCs concentrations were monitored (more details about the measurements are shown in Table S1). Hourly observations of conventional meteorological parameters, such as temperature, pressure, relative humidity, wind direction, and wind speed, were sourced from the European Centre for Medium-Range Weather Forecasts (ECMWF). The planetary boundary layer height (PBLH) data used in the model here was obtained from the web portal of the Real-time Environmental Applications and Display sYstem (READY) of the National Oceanic and Atmospheric Administration (NOAA) Air Resource Laboratory (https://ready.arl.noaa.gov/READYamet.php).

2.2 Box model simulation

This study employed an observation-constrained zero-dimensional photochemical reaction model (Observed 0-D box model) to simulate atmospheric photochemical processes. The chemical mechanism module is the core of the box model, and most mainstream studies use the Master Chemical Mechanism (MCM) nested within the model, incorporating processes such as solar radiation, boundary layer height, atmospheric photochemistry, and dry deposition (Zhang et al., 2022). The OBM model used in this study is AtChem2 (https://atchem.leeds.ac.uk/webapp/), which is equipped with the Master Chemical Mechanism (MCM v3.3.1: https://mcm.york.ac.uk/MCM) to simulate O_3 and radical chemistry and analyze their budgets (Wang et al., 2022a; Sommariva et al., 2020). The model includes approximately 143 VOCs, 6,700 chemical species, and over 17,000 reactions. Hourly resolution observational data of O_3, NO, NO_2, CO, SO_2, HONO, VOCs (in total 82 species), meteorological parameters (e.g., temperature, relative humidity, pressure, and boundary layer height), and photolysis rates were used as model constraints. The constraints are applied to the model every 1 h, with no free concentration evolution in between. Photolysis rates for unmeasured species were calculated using the Tropospheric Ultraviolet and Visible Radiation Model (TUV v5.3) (Table S2). Additionally, to avoid unreasonable increases in the concentrations of constrained species, a dilution rate of 1/86400 s^{-1} was applied. Before the simulation, the model underwent a 48-hour pre-run to stabilize unmeasured species (e.g., radicals).

The configuration of model mechanisms was informed by previous research, with a particular focus on the dry deposition processes of key species (e.g., O_3, NO_2, SO_2, H_2O_2, HNO_3, PAN, and HCHO), the heterogeneous uptake reactions of HO_2 and N_2O_5, and the Cl· chemistry mechanism. Dry deposition is a critical pathway for the transfer of atmospheric pollutants from the gas phase to the Earth's surface, significantly influencing the concentration distribution and removal of regional pollutants. Many models have already incorporated this atmospheric physical process (Ma et al., 2022; Chen et al., 2020a). Although the heterogeneous uptake of HO_2 is not the dominant loss pathway of HO_2, it accounts for approximately 10–40 % of global HO_2 loss (Li et al., 2019); as a termination reaction, its direct impact on photochemical O_3 production is non-negligible. Studies have shown that including the heterogeneous uptake mechanism of HO_2 in simulations reduces $P(O_3)_{net}$ concentration and alters the sensitivity to VOCs (Zhou et al., 2021; Dyson et al., 2022). Additionally, Cl· enhances atmospheric oxidation, accelerating the OH-HO_2-RO_2 reaction cycle (Ma et al., 2023). By incorporating these mechanisms, this study aims to more accurately simulate the atmospheric chemical processes and their impacts on pollutant concentrations in the PRD region (Zhou et al., 2024a). The configurations of each scenario are as follows: Case A considers only the simplified chemical reaction mechanism from the MCM, excluding dry deposition and heterogeneous reactions; Case B incorporates the HO_2 uptake by ambient aerosols based on Case A; Case C further includes the dry deposition processes of key species on top of Case B; and Case D_1 extends Case C by adding the N_2O_5 uptake mechanism and Cl· related photochemical reactions. Detailed simulation parameter settings can be found in our previous study (Zhou et al., 2024a) and the supplementary information (Table S3).

2.3 Model performance evaluation

The Index of Agreement (IOA) was used to evaluate the simulation performance (Li et al., 2021).

$$IOA = 1 - \frac{\sum_{i=1}^{n} (O_i - S_i)^2}{\sum_{i=1}^{n} (|O_i - \overline{O}| - |S_i - \overline{O}|)^2} \tag{7}$$

where O_i and S_i represent the observed and simulated values, respectively, $\overline{O}$ denote the mean of the observed values, and n is the number of samples. The IOA ranges from 0 to 1, with higher values indicating better agreement between observed and simulated values. In addition to the IOA, the Pearson correlation coefficient (R), mean bias (MB), normalized mean bias (NMB), root mean square error (RMSE), mean fractional bias (MFB) and mean fractional error (MFE) were used to evaluate the consistency between observed and simulated values (Table S7).

2.4 k_{OH}

Total OH reactivity (k_{OH}) is a crucial indicator of atmospheric chemical cycling and oxidative capacity (Gilman et al., 2009). k_{OH} is defined as the sum of the products of the concentrations of all reactive species X_i that can react with OH radicals and their respective reaction rate constants, calculated as follows:

$$k_{OH} = \sum_i k_{OH+X_i} \cdot [X]_i \tag{8}$$

where X_i includes CO, NO_X, and VOCs, among others, and k_{OH+X_i} is the reaction rate constant (s^{-1}) between reactive species X_i and OH radicals.

2.5 OFP

O_3 Formation Potential (OFP) is an indicator used to measure the relative contribution of different VOC species to ground-level O_3 formation (Wu et al., 2020). The formula for OFP is as follows:

$$\mathrm{OFP} = [\mathrm{VOCs}]_i \times \mathrm{MIR}_i \tag{9}$$

where $[VOCs]_i$ represents the concentration of a specific VOC species i (μg m^{-3}), and MIR represents the maximum incremental reactivity of the VOC species i (g_{O_3}/g_{VOC}). MIR is used to characterize the increase in O_3 production per unit increase in VOCs under conditions where O_3 formation is most sensitive to VOCs.

2.6 Absolute $P(O_3)_{net}$ sensitivity

We calculated the modelled OFS using the absolute $P(O_3)_{net}$ sensitivity, adapted from the logarithmic derivative approach of Sakamoto et al. (2019). It is defined as the change in $P(O_3)_{net}$ with respect to the natural logarithm of O_3 precursor concentrations. This method facilitates the quantitative assessment of how reductions in O_3 precursors contribute to the overall reduction of $P(O_3)_{net}$ over a period or within a region. The formula is as follows:

$$\text{Absolute } P(O_3)_{net} = \frac{dP(O_3)_{net}}{d\ln[X]} \tag{10}$$

In the equation, $[X]$ represents NOx or VOCs. A positive absolute $P(O_3)_{net}$ sensitivity indicates that reducing the precursor will lead to a decrease in the $P(O_3)_{net}$. In contrast, a negative value indicates that reducing the precursor will lead to an increase in the $P(O_3)_{net}$ (Dyson et al., 2022). In this study, the analysis of absolute $P(O_3)_{net}$ sensitivity was conducted using the box model through an analytical calculation approach that does not involve artificial perturbation of precursor concentrations.

3 Results and discussion

3.1 Overview of observation campaign

The Supplementary Materials (SM, Fig. S3, S4, and Table S4, S5) provide the time series plots, diurnal variation, and daytime averages (daytime: 6:00-18:00) of meteorological parameters, conventional pollutants, photolysis rate constants, NO, $P(O_3)_{net}$ and hourly VOCs concentrations from 4–26 October 2023, at the Guangdong Atmospheric Supersite of China. The site was located downwind of the Guangzhou-Foshan area, with atmospheric pollutants primarily originating from the northeast. To access daily O_3 pollution levels, the maximum daily 8-hour average O_3 concentration (MDA8) was employed, in accordance with the Technical Specification for Ambient Air Quality Evaluation (Trial) (HJ 663-2013). In this study, days with MDA8-O_3 concentration exceeding the Class II limit stipulated by the Ambient Air Quality Standards (GB3095-2012) were defined as O_3 pollution days (with MDA8-O_3 concentration limit of 160 $\mu g\ m^{-3}$ (equivalent to approximately 81.6 ppbv at 25°C), while others were defined as normal days.

During the whole observation period, there were 6 O_3 pollution days (15–17 and 24–26 October 2023). The maximum O_3 mixing ratio (136.5 ppbv) occurred at 15:00 on 25 October 2023, while the maximum $P(O_3)_{net}$ (53.7 ppbv h^{-1}) occurred at 10:00 on 24 October 2023. Diurnal variation plots show that O_3 and $P(O_3)_{net}$ exhibited single-peak patterns, with O_3 peaking at 15:00 and $P(O_3)_{net}$ peaking between 9:00-10:00. On O_3 pollution days, the daytime average mixing ratios concentrations of O_3 and $P(O_3)_{net}$ during the observation period were 63.2 ± 37.6 ppbv and 14.4 ± 13.8 ppbv h^{-1}, respectively, both approximately twice as high as on normal days (daytime average O_3: 30.9 ± 22.9 ppbv; daytime average $P(O_3)_{net}$:7.2 ± 9.4 ppbv h^{-1}). The maximum values of directly measured $P(O_3)_{net}$ in different ambient environments in previous studies are listed in Table S6, ranging from 10.5 to 100 ppbv h^{-1}, and the measured $P(O_3)_{net}$ values in this study fall within this range, demonstrating the reasonableness of the values measured in this study.

As shown in Fig. S4, the diurnal variation of parameters on O_3 pollution days and normal days indicates that the nighttime background concentrations/mixing ratios of O_3 precursors (TVOC and NO_X) are higher on O_3 pollution days. However, during the period of strongest sunlight (11:00-14:00), the concentrations/mixing ratios of TVOC and NO_X on O_3 pollution days are lower than those on normal days. Specifically, on O_3 pollution days, the TVOC concentration is 11.4 μg m^{-3}, and the NO_X concentration is 13.5 ppbv, while on normal days, the TVOC concentration is 13.7 μg m^{-3}, and the NO_X concentration is 14.8 ppbv. As the PBLH on O_3 pollution days and normal days does not differ statistically during the period of strongest solar radiation (11:00-14:00, *t-test*, p=0.45, see Fig. S4k), the lower daytime concentrations/mixing ratios of O_3 precursors on O_3 pollution days than on normal days may be due to higher photolysis rates on O_3 pollution days (see Fig. S4a). The diurnal variation of NO concentration on O_3 pollution days showed an early morning peak at 8:00, rising to 12.2 ppbv and then decreasing to 1.6 ppbv. By comparing the diurnal variation data between O_3 pollution days and normal days, we found that both O_3 mixing ratios and $P(O_3)_{net}$ values were significantly higher on O_3 pollution days, particularly during the daytime (6:00-18:00). This phenomenon aligns with the conclusion that high temperatures, low humidity, strong radiation, and stable weather conditions favor O_3 pollution formation.

3.2 Characteristics of VOC concentrations and composition

This study analyzed 110 VOC species, examining the contributions of different categories to TVOC concentrations, k_{OH}, and daily OFP. We also identified the top 10 VOC species contributing to these three indicators (Fig. S5), aiming to explore the atmospheric presence, chemical reactivity, and environmental impact of VOCs. Additionally, this study used two classification methods to group VOC species. Method 1 divided VOCs into alkynes (1 species), alkanes (27 species), alkenes (11 species), aromatic hydrocarbons (17 species), OVOCs (20 species), halogenated hydrocarbons (33 species), and sulfur-containing VOCs (1 species). Method 2 categorized VOCs into BVOC (Biogenic Volatile Organic Compounds), OVOCs (Oxygenated Volatile Organic Compounds), and AVOCs/NMHC (Anthropogenic Volatile Organic Compounds), with specific classifications shown in Table S4.

During the observation period, the daily average TVOC concentration ranged from 7.2 to 28.9 μg m^{-3}. OVOCs contributed the most (40.8 %), followed by halogenated hydrocarbons (20.8 %), aromatic hydrocarbons (18.3 %), alkanes (17.9 %), alkenes (1.7 %), and alkynes (0.5 %). The k_{OH} average value was 12.1±3.9 s^{-1}, primarily contributed by OVOCs (62.9 %), followed by halogenated hydrocarbons (10.8 %), alkenes (10.4 %), aromatic hydrocarbons (9.8 %), alkanes (6.0 %), and alkynes (0.1 %). Among the alkenes in the known MCM mechanism, ethylene, as an indicator of VOCs, had the highest proportion, accounting for 10.7 % of alkenes k_{OH} and 2.8 % of NMHC k_{OH}. Formaldehyde, another VOCs indicator, was the most dominant species in OVOCs k_{OH}, contributing about 13.3 %. Among VOC species, OVOCs contributed the most to OFP (51.6 %), followed by aromatic hydrocarbons (32.9 %), alkenes (8.0 %), alkanes (6.9 %), halogenated hydrocarbons (0.5 %), and alkynes (0.2 %). The analysis results show that although halogenated hydrocarbons dominate VOCs concentration emissions, their contribution to O_3 pollution is low. In contrast, alkenes, despite their lower contribution to VOCs concentration emissions, are important precursors for O_3 formation. Based on the comprehensive analysis of VOCs concentration, $k_{OH,}$ and OFP, OVOCs and aromatic hydrocarbons significantly contribute to O_3 formation and should be prioritized as key VOC species for O_3 pollution control in the PRD region. This result aligns with other related studies in the PRD, such as those in Shenzhen (Yu et al., 2020; Guanghe et al., 2022), Guangzhou (Pei et al., 2022), and Jiangmen (Jing et al., 2024), which indicate that OVOCs and aromatic hydrocarbons are key VOC species for O_3 formation. As OVOCs arise from both direct (anthropogenic and natural) emissions and secondary atmospheric formation (Lyu et al., 2024; Yuan et al., 2012), precluding a direct quantification of their respective contributions to O_3 formation. Nevertheless, our previous work showed that anthropogenic primary VOCs correlate most closely with instantaneous $P(O_3)_{net}$ on O_3 pollution days, and urban anthropogenic OVOC emissions markedly enhance both oxidative capacity and O_3 production (Qian et al., 2025; Wang et al., 2024b).

Overall, toluene, m/p-xylene, formaldehyde, 2-hexanone, ethyl acetate, and tetrahydrofuran consistently ranked in the top 10 VOC species in terms of concentration, k_{OH} and OFP contribution. These VOC species mainly originate from human activities, such as industrial production, solvent use, traffic emissions, and fuel combustion, highlighting the significant impact of anthropogenic sources on O_3 pollution (Cai et al., 2010; Yang et al., 2023; Zheng et al., 2019).

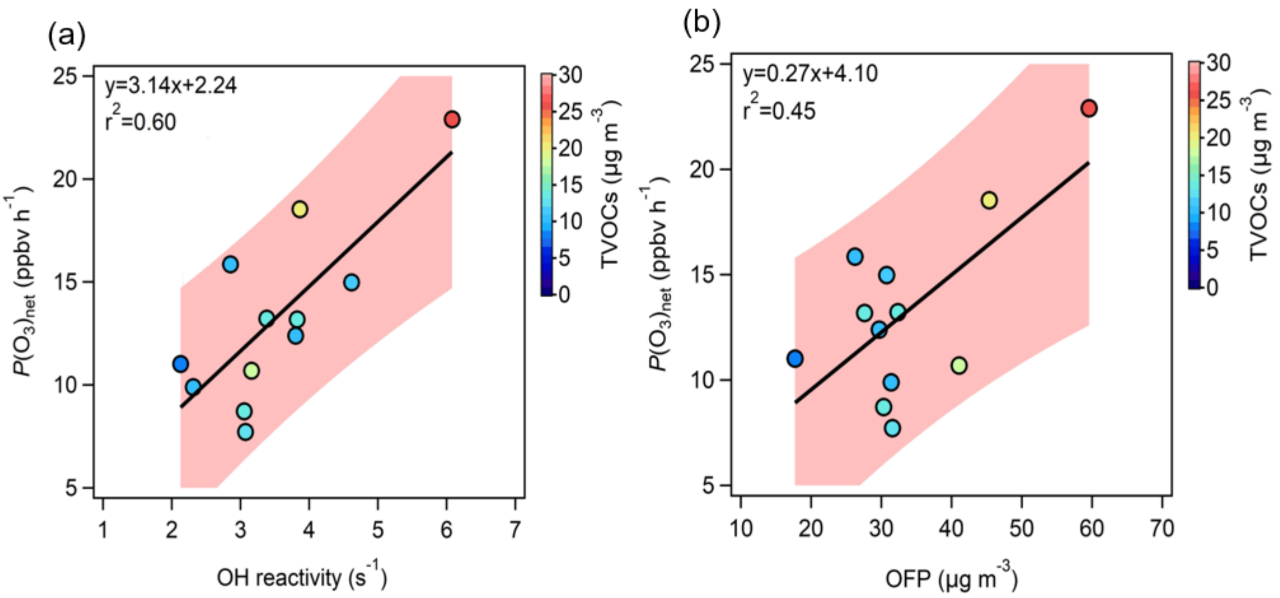

Figure 1: Correlation between measured $P(O_3)_{net}$ ($P(O_3)_{net_}$Mea) and (a) total OH reactivity (k_{OH}) and (b) O_3 Formation Potential (OFP). The shaded area in the figure represents the confidence interval (90 %) of the fitting line between $P(O_3)_{net}$ and k_{OH}, and between $P(O_3)_{net}$ and OFP.

Figure 1 shows the correlation between $P(O_3)_{net_}$Mea and k_{OH} and OFP (calculated using the daytime average data during the observation period). Data outside the confidence interval may be due to the fact that the calculation of k_{OH} and OFP did not fully consider the environmental conditions and atmospheric chemistry complexity at the observation site (Zhang et al., 2024; Yadav et al., 2024). The color of the scatter points represents the TVOC concentration. The r^2 values between $P(O_3)_{net}$ measurements and k_{OH} and OFP are 0.6 and 0.5, respectively, indicating that VOCs with higher k_{OH} and OFP significantly enhance the $P(O_3)_{net}$.

3.3 Comparison and optimization of simulated and measured $P(O_3)_{net}$ values

Based on our previous research (Zhou et al., 2024a), we named the scenario considering only the current chemical reaction mechanism from the MCM v3.3.1 in the box model as Case A. Subsequently, we gradually incorporated the HO_2 uptake by ambient aerosols, dry deposition, N_2O_5 uptake, and $ClNO_2$ photolysis mechanisms into the MCM mechanism in the box model, implemented as modelling scenarios labeled Case B, Case C, and Case D_1. The specific parameter settings for each scenario are shown in Table S3. The time series and diurnal variations of the $P(O_3)_{net}$_Mea and $P(O_3)_{net}$_Mod for Cases A–D_1 are shown in Fig. S7. To evaluate the model's performance, $P(O_3)_{net}$_Mea and $P(O_3)_{net}$_Mod data were used to calculate IOA, R, MB, NMB, RMSE, MFB and MFE values under different scenarios (Table S7). The IOA values between $P(O_3)_{net}$_Mod and $P(O_3)_{net}$_Mea was > 0.86 for all cases, and R ranged from 0.84 to 0.98, indicating that the model can reasonably reproduce the variations in $P(O_3)_{net}$. However, MB and NMB were −3.0 to −2.4 ppbv h^{-1} and −30.5 % to −24.9 %, respectively, revealing a systematic underestimation of $P(O_3)_{net}$. RMSE ranged from 7.0 to 7.2 ppbv h^{-1}, while MFB and MFE ranged from −3.1 % to −1.7 % and 53.8 % to 55.5 %, respectively. These results suggest that, although the model captures the overall trends well, there is room to reduce simulation biases.

In all modelling scenarios from Case A–Case D_1, $P(O_3)_{net}$_Mod values were generally lower than $P(O_3)_{net}$_Mea (see Fig. 3). Although the correlation between $P(O_3)_{net}$_Mea and $P(O_3)_{net}$_Mod was good (Fig. S9, r^2=0.73), even after incorporating mechanisms that may affect O_3 production simulation biases into to the box model (labeled as Case D_1), the simulated daytime average $P(O_3)_{net}$_Mod was still 3.4 ppbv h^{-1} lower than $P(O_3)_{net}$_Mea (26.3 % bias), with a peak deviation of up to 13.3 ppbv h^{-1} (44.8 %), as shown in Fig. 2. We defined the difference between $P(O_3)_{net}$_Mea and $P(O_3)_{net}$_Mod as $P(O_3)_{net}$_Missing, and its distribution of each day is shown in Fig. S10. Due to the measurement error of HONO by MARGA in this study, the modelled $P(O_3)_{net}$ tends to be underestimated (as shown in SM: S2); thus, we define the $P(O_3)_{net}$_Missing obtained from all simulation cases as the upper-limit values. During the observation period, 7–10 October and 18–22 October were rainy days, with a median $P(O_3)_{net}$_Missing < 1.1 ppbv h^{-1}; therefore, these days were excluded when calculating the diurnal variations of different O_3 production and consumption pathways. On non-rainy days, the averaged daytime $P(O_3)_{net}$_Missing reached 4.5 ± 7.6 ppbv h^{-1}, accounting for 31% of the total measured $P(O_3)_{net}$. Furthermore, the enlarged days in Fig. 2 reveal day-to-day variations in $P(O_3)_{net}$_Mod across the different cases, underscoring that the overall diurnal pattern described above does not resolve this variability. The averaged daytime $P(O_3)_{net}$_Missing values on O_3 pollution days were statistically higher than those on normal days (*t-test*, p<0.05), suggesting that while the supplementary mechanisms explored in the model may contribute to some extent, they are unlikely to be the dominant cause of the $P(O_3)_{net}$_Missing.

We further explore the possible reasons for the discrepancies between $P(O_3)_{net}$_Mea and $P(O_3)_{net}$_Mod using the modelling results of Case D_1. The ratio of cumulative $P(O_3)_{net}$_Mea and $P(O_3)_{net}$_Mod derived from Case D_1 was 1.4, calculated by summing the daytime data with 1 h resolution during the observation period. This result is consistent with previous findings: Cazorla and Brune (2009) reported a ratio of 1.3, and Ren et al. (2013) and Hao et al. (2023) both reported 1.4. As shown in Fig. 2, the HO_2+NO reaction dominates O_3 production, accounting for 71.4 % of total O_3 production pathways. In contrast, the main O_3 loss pathways were $OH+NO_2$ and RO_2+NO_2, accounting for 67.9 % and 16.5 % of total O_3 consumption pathways, respectively. The importance of the HO_2/RO_2 reaction pathways indicates that simulation biases in HO_2 or RO_2 will propagate into $P(O_3)_{net}$_Mod.

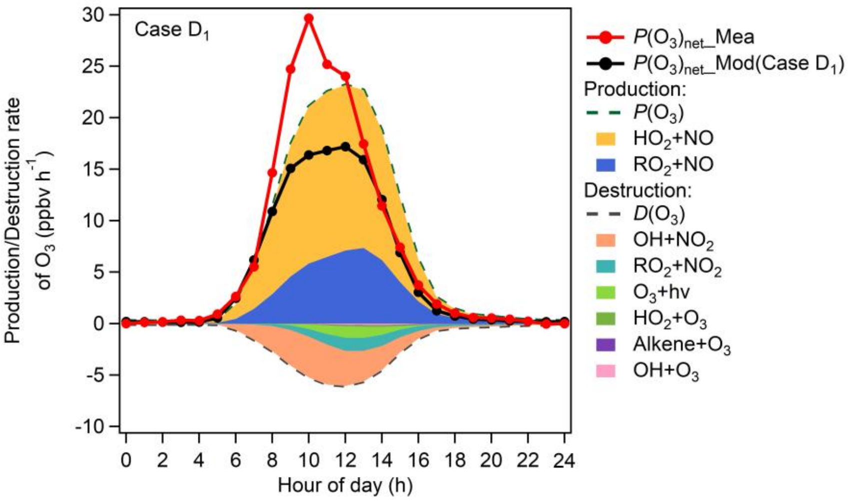

Figure 2: Diurnal variations (excludes rainy days) of O_3 production and destruction rates modelled in Case D_1, and measured ($P(O_3)_{net}$_Mea) and modelled ($P(O_3)_{net}$_Mod) $P(O_3)_{net}$.

To explore the possible drivers of $P(O_3)_{net}$_Missing, we correlated it with TVOC, NO_X, J_{O1D}, T, and O_X separately for O_3 pollution days and normal days (Fig. S11). On O_3 pollution days, $P(O_3)_{net}$_Missing exhibited a moderate positive correlation with VOCs (r^2 =0.4, R=0.2, t=2.9) and NO_X (r^2=0.5, R=0.2, t=3.8), confirming that the $P(O_3)_{net}$_Missing is larger at higher precursor concentrations/mixing ratios (both t > critical 2.0, $p < 0.05$), consistent with earlier box-model studies (Whalley et al., 2021; Ren et al., 2013; Zhou et al., 2024a). A moderate positive correlation is also found with J_{O1D} on both O_3 pollution days and normal days, with r^2 values of 0.5 and 0.4, respectively. On normal days all correlations collapse ($r^2 < 0.2$, $p > 0.1$), implying that the model deficit is not tied to the measured precursors under low-NO_x conditions and may instead related to the missing mechanisms for unmeasured photolabile VOCs. Wang et al. (2022b) indicates that constraining OVOCs in the model is crucial for the accuracy of $P(O_3)_{net}$_Mod, and photochemical models without OVOCs constraints significantly underestimate $P(O_3)_{net}$. In our previous study on the industrial city of Dongguan (Zhou et al., 2024a), we used parameter equations developed by Wang et al. (2024a; 2024b) to quantify the impact of missing k_{OH} on $P(O_3)_{net}$_Missing and qualitatively tested the potential compensating effects of unmeasured OVOCs on $P(O_3)_{net}$_Missing. This study measured more VOC species compared to the Dongguan campaign (Table S4). Therefore, we further compensate for the Case D_1 scenario by constraining more measured VOC species compared to the study in Dongguan (e.g., OVOCs, halogenated hydrocarbons) to explore their impact on $P(O_3)_{net}$_Mod. The specific simulation scenario settings are described in Table S3.

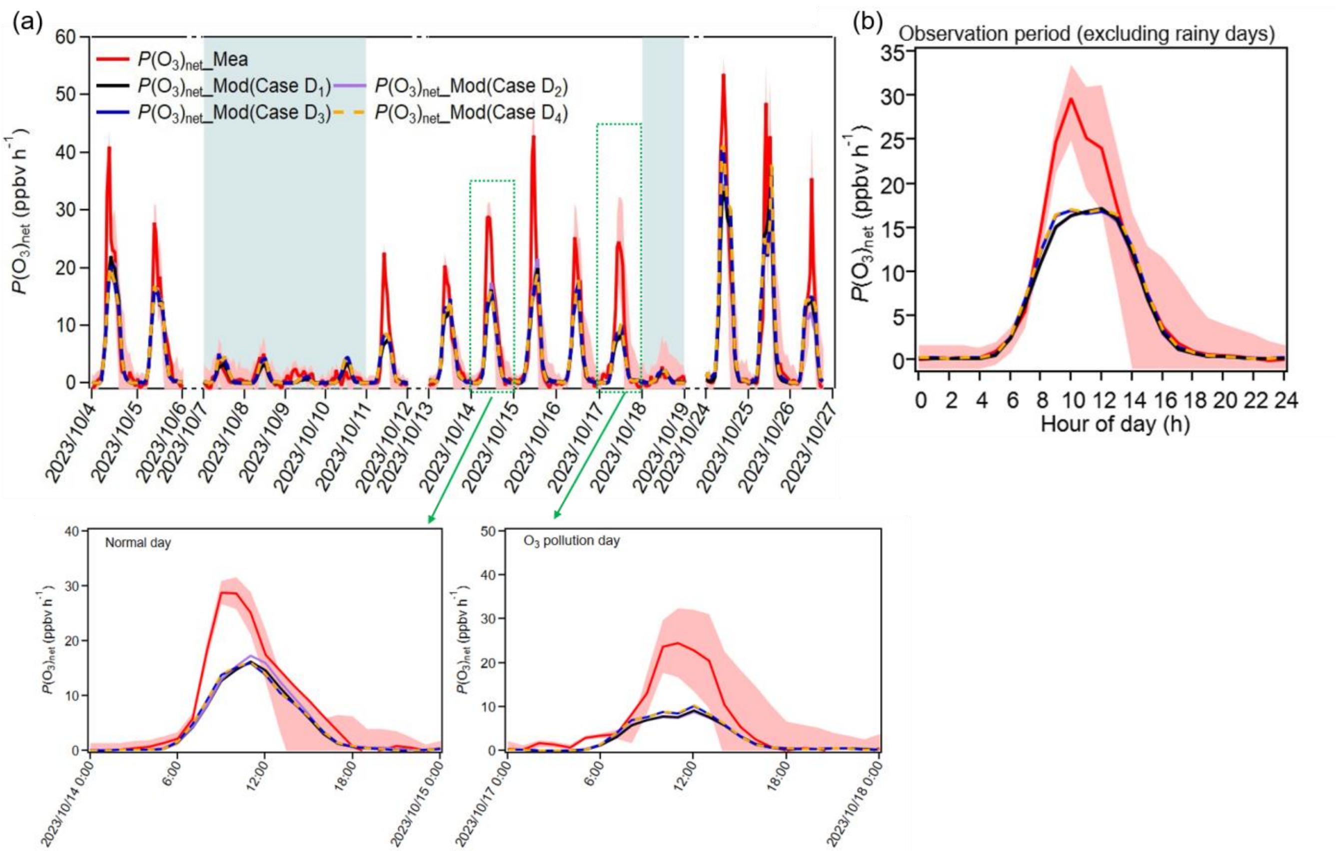

Figure 3: The time series and diurnal variations of $P(O_3)_{net}$_Mea and $P(O_3)_{net}$_Mod (Case D_1–D_4) during the observation period, with an enlarged view for an O_3 pollution day (October 26, 2023) and a normal (O_3 non-pollution) day (October 14, 2023); The shaded areas in (a) represent rainy days.

Figure 3 shows the time series and diurnal variations of $P(O_3)_{net}$_Mea and $P(O_3)_{net}$_Mod (under Case D_1–D_4) during the observation period. Specifically, we added constraints for measured acetaldehyde, acrolein, acetone, and butanone (OVOCs, which were considered as potential contributors for $P(O_3)_{net}$_Missing in Dongguan) to the model based on Case D_1, which is labeled as Case D_2. However, the daytime mean $P(O_3)_{net}$_Mod in Case D_2 decreased by 0.5 % compared with Case D_1, indicating that the dominant OVOC species responsible for $P(O_3)_{net}$_Missing may differ between Heshan and Dongguan. We further constrained all measured OVOC species in Heshan (which included additional OVOCs species compared to that added to Case D_2, such as propionaldehyde, butyraldehyde, and valeraldehyde) that could be input into the box model in the Case D_3 simulation scenario (more details can be found in Table S8). The results showed that the averaged daytime $P(O_3)_{net}$_Mod from Case D_3 increased by 4.4 % compared to that in Case D_2. Notably, in Case D_3, constraining all OVOC species significantly improved $P(O_3)_{net}$_Mod during the morning period (8:00-9:00), with an increasing rate of approximately 10.2 % (~1.3 ppbv h$^-$

^{1}). Additionally, Case D_4 scenario added constraints for chlorine-containing VOCs (i.e., all measured VOC species listed in Table S8 that could be input into the OBM model were constrained). The daytime average $P(O_3)_{net_}$Mod values from Case D_4 changed by only 1.1 % compared to those derived from Case D_3, indicating that the potential contribution of OVOCs to compensating $P(O_3)_{net_}$Missing is greater than that of chlorine-containing VOCs. The negligible (or even negative) change in $P(O_3)_{net_}$Mod when OVOCs are constrained in Cases D1-D4 may arise because the OVOC constraint masks deficiencies in the model's chemcial mechanism and artificially suppresses diagnostic signals of missing secondary formation pathways. Until the underlying chemical mechanisms are improved, observational nudging of OVOCs offers a practical compromise—it helps maintain concentration accuracy while limiting unrealistic chemical feedbacks (more details can be found in Supplementary Materials S5). However, in modelling scenario Case D_4, the daytime average $P(O_3)_{net_}$Mod still showed a 22.2 % underestimation compared to the measured values. Accurate quantification of $P(O_3)_{net}$ missing is possible here because the diurnal patterns of measurement uncertainty and the modelling bias responsible for the $P(O_3)_{net}$ missing do not co-vary; consequently, measurement uncertainty is much smaller than modelling bias for most of the daytime, especially around noon.

The diurnal variations of O_3 production pathways in Case D_4 are shown in Fig. S12. Compared to Case D_1, the RO_2+NO reaction rate in Case D_4 was higher by 0–2.1 ppbv h^{-1} in the diurnal variations during the whole measurement period (excluded the rainy days). The RO_2 species with higher contributions to this pathway included CH_3O_2, $HO_2C_4O_2$, $HO_{13}C_4O_2$, $HOCH_2CH_2O_2$, HO_3C4O_2, $CH_3COCH_2O_2$, and $COCCOH_2CO_2$. This indicates that the constraints on additional OVOCs in Case D_4 (such as aldehyde and ketone compounds with specific functional groups, e.g., carbonyl and hydroxyl) increased the intermediate RO_2 products, leading to a significant enhancement in the RO_2+NO reaction rate. This suggests their large potential to contribute to $P(O_3)_{net_}$Missing.

The modelling results of scenarios Case D_1–D_4 show that although constraining the measured VOC species in the box model mechanism can reduce $P(O_3)_{net_}$Missing to some extent, there is still a significant gap between the simulated and measured $P(O_3)_{net}$ values. Previous studies have shown that the RO_2 isomerization (Crounse et al., 2012), autoxidation (Wang et al., 2017), and the accretion reactions (Berndt et al., 2018) can also effect modelled $P(O_3)_{net}$, but these processes have not been investigated here. Also, the potential contribution of unmeasured VOC species to compensating $P(O_3)_{net_}$Missing in the box model mechanism cannot be ignored. Yang et al. (2017) and Tan et al. (2019) conducted radical measurements at the Guangdong Atmospheric Supersite of China in autumn of 2014, revealing missing k_{OH} contributions of approximately 32 % and 50 %, respectively. Yang et al. (2017) pointed out that the missing k_{OH} contributions in the Heshan region may originate from OVOCs such as aldehydes, acids, and dicarbonyls. Tan et al. (2019) indicated that about 60 % of the O_3 produced in the Heshan region was contributed by unmeasured VOCs. We hypothesize that the remaining $P(O_3)_{net_}$Missing is caused by unknown VOCs that are not constrained in the box model.

The method of estimating missing VOC concentrations through the empirical linear relationship between OH reactivity (k_{OH}) and $P(O_3)_{net}$ is used in this study, the scientific basis lies in the fact that $P(O_3)_{net}$ is closely related to the production rate of RO_X radicals ($P(RO_X)$), which are primarily formed through the reaction of OH with VOCs. Since $P(RO_X)$ is directly influenced by the OH reactivity (k_{OH}), $P(O_3)_{net}$ is consequently correlated with k_{OH}. Previous study has shown that $P(O_3)_{net}$

exhibits a linear relationship with both $P(\mathrm{HOx})$ and k_{OH} when O_3 formation is located in VOCs-limited regime (Baier et al., 2017), and this approach reflects nearly actual atmospheric chemistry if $P(O_3)_{\mathrm{net}}$ missing is driven by VOCs reactivity missing (Wang et al., 2024b). Furthermore, we examined whether unconstrained secondary products affect $P(O_3)_{\mathrm{net}}$ missing —and thus the linear relationship between $P(O_3)_{\mathrm{net}}$ missing and k_{OH}—by analysing its dependence on the ethylbenzene/m,p-xylene ratio. Because this ratio increases with the degree of air-mass aging (de Gouw et al., 2005; Yuan et al., 2013), the observed decrease in the $P(O_3)_{\mathrm{net}}$ missing with increasing ratio (Fig. S11f) indicates that the $P(O_3)_{\mathrm{net}}$ missing is not likely caused by unaccounted secondary production. By quantifying the relationship between k_{OH} and $P(O_3)_{\mathrm{net}}$, the contribution of missing k_{OH} ($k_{\mathrm{OH\_}}$ Missing) to $P(O_3)_{\mathrm{net_}}$Missing can be assessed, and compensating for $k_{\mathrm{OH\_}}$ Missing in the box model can help reduce $P(O_3)_{\mathrm{net_}}$Missing. Figure 4 shows the relationship between k_{OH} and $P(O_3)_{\mathrm{net_}}$Mod calculated under the Case D_1 scenario, which can be expressed as:

$$P(O_3)_{net_{Missing}} = 3.4 \times k_{OH_{Missing}} - 2.7 \tag{11}$$

where $P(O_3)_{\mathrm{net_}}$Missing and $k_{\mathrm{OH\_}}$ Missing in the equation represent the daytime averaged values for each day. Based on this relationship, we calculated $k_{\mathrm{OH\_}}$ Missing according to calculated $P(O_3)_{\mathrm{net_}}$Missing for each day. This value was then used to compensate for the unmeasured VOCs in the model (with a daytime k_{OH} compensation range of 1.2–2.4 s^{-1}, approximately 27.6–45.1% of missing values). Based on the significant contribution of OVOCs to $P(O_3)_{\mathrm{net_}}$Missing mentioned earlier, we designed three modelling scenarios to compensate for $k_{\mathrm{OH\_}}$ Missing, with the specific multiples varying each day. We note that these scenarios are idealized sensitivity tests to explore potential bounds of OVOCs' contribution to $P(O_3)_{\mathrm{net_}}$Missing compensation, rather than realistic emission assumptions. Specifically, we tested how much the $P(O_3)_{\mathrm{net_}}$Missing could be accounted for if the k_{OH} were attributed to different VOCs categories. The specific scenarios include: (1) Case E_1: by expanding the constrained overall VOCs concentrations in Case D_1 (daily mean compensation range for TVOCs: 0.5–2.8 μg m^{-3}) the daily TVOC concentration was increased by 1.1 to 1.7 times; (2) Case E_2: according to k_{OH} ratio of NMHC to OVOCs in the constrained VOCs of Case D_1, the concentrations of ethylene (a representative NMHC species) and formaldehyde (OVOCs indicator) were expanded separately. The ethylene concentration (daily mean compensation range for TVOCs: 0.5–2.8 μg m^{-3}) was increased by 5.9 to 85.6 times, and the formaldehyde concentration (daily mean compensation range for TVOCs: 0.0–0.5 μg m^{-3}) was increased by 1.4 to 2.0 times; (3) Case E_3: by expanding only the formaldehyde concentration to compensate for $k_{\mathrm{OH\_}}$ Missing, in this case, the daily formaldehyde concentration (daily mean compensation range for TVOCs: 0.6–1.4 μg m^{-3}) was increased by 1.8 to 9.2 times, to verify the role of OVOCs in compensating for $P(O_3)_{\mathrm{net_}}$Missing. The time series and overall diurnal variations of modelled Cases E1-E3 are presented alongside Case D1 in Fig. 5.

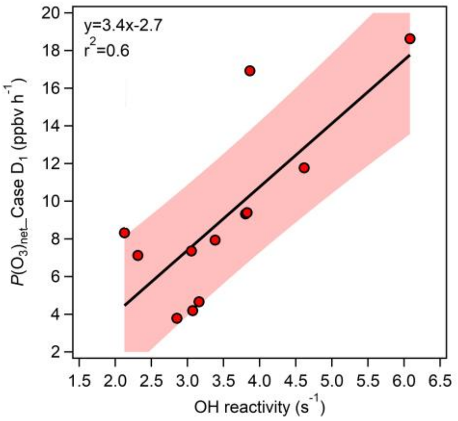

Figure 4: The relationship between k_{OH} and $P(O_3)_{net}$_Mod calculated under the Case D_1 scenario (using the daily daytime average values during the observation period).

In Case E_1, where the overall TVOC concentration was increased to compensate for k_{OH}_Missing without distinguishing VOCs categories, the compensation effect was limited due to the dilution effect of low-reactivity VOCs, resulting in a reduction of the daytime average $P(O_3)_{net}$_Missing proportion from 26.3 % (calculated as $P(O_3)_{net}$_Missing/$P(O_3)_{net}$_Mea) to 10.3 %. In Case E_2, where the concentrations of ethylene and formaldehyde were expanded to compensate for k_{OH}_Missing, the daytime average $P(O_3)_{net}$_Missing proportion reduced from 26.3 % to 17.2 %. This proportion is higher than that obtained from Case E1, which may be due to the relatively low reactivity of ethylene limited the overall compensation effect. In contrast, Case E_3 compensated for k_{OH}_ Missing solely by expanding the formaldehyde concentration. More details concerning the cases settings are shown in Table S3. Since formaldehyde, as a representative high-reactivity OVOC species, contributes more directly and significantly to O_3 generation through photochemical pathways (Mousavinezhad et al., 2021), it achieved the best compensation effect, reducing the daytime average of $P(O_3)_{net}$_Missing from 26.3 % to 5.1 %. However, $P(O_3)_{net}$_Missing during the peak period of diurnal variation remained at 9.0 ppbv h^{-1}. This result confirms the critical role of high-reactivity OVOCs (especially those with the same photochemical reaction characteristics as formaldehyde) in compensating for $P(O_3)_{net}$_Missing. Further, it suggests the potential presence of other unmeasured high-reactivity VOC species in the ambient atmosphere. Constraining these species could help further improve the model's simulation accuracy (Lyu et al., 2024; Wang et al., 2024b). Overall, the degree of compensation for $P(O_3)_{net}$_Missing follows the order Case E_3>Case E_1>Case E_2, which may be related to the reactivity of the selected VOCs. However, we observe a slight difference in the diurnal trends of $P(O_3)_{net}$ across different days (enlarged view in Fig. 5); this depicts the overall pattern for the observation period described above does not capture day-to-day variability.

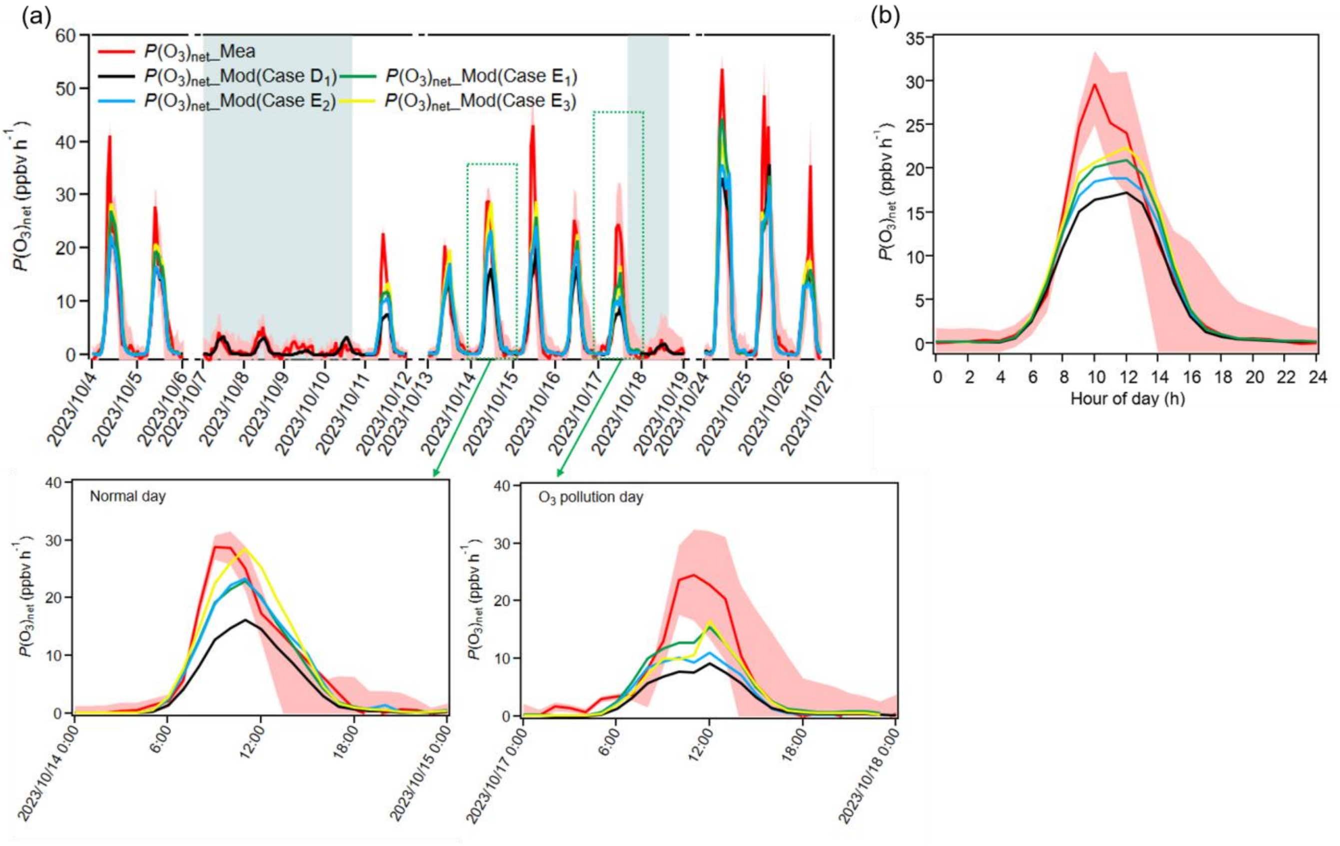

Figure 5: (a) Time series and (b) diurnal variations of $P(O_3)_{net}$_Mea and $P(O_3)_{net}$_Mod (Case D_1–E_3) during the observation period, with an enlarged view for an O_3 pollution day (October 26, 2023) and a normal (O_3 non-pollution) day (October 14, 2023); (b) Diurnal variations excluding rainy days. The shaded areas in (a) represent rainy days.

4. OFS assessment based on measurements and simulations

This study systematically estimated OFS during the observation period (4–5, 11, 13–17, and 24–26 October 2023) using measured OFS (see Sect. 2.1) and modelled OFS (see Sect. 2.6). The time series of measured $P(O_3)_{net}$_Mea, $P(O_3)_{net}^{+NO}$ and $P(O_3)_{net}^{+VOCs}$ based on sensitivity experiments using the NPOPR detection system are shown in Fig. S13. We see the measurement uncertainty decreased with increasing $P(O_3)_{net}$ values: it reaches approximately 23% when $P(O_3)_{net}$ is around 0 ppbv h^{-1}, but falls below 3% when $P(O_3)_{net}$ is around 50 ppbv h^{-1}. Fig. S14 shows the diurnal variation of the directly measured IR index compiled from all 11 days of OFS experiments, together with the absolute $P(O_3)_{net}$ sensitivity to NO_X and VOCs calculated with the box model (Case D_1, Eq. (10)). It therefore depicts the overall trend across the observation period and does not reflect the day-to-day variability. We see that both measured OFS and modelled OFS captured the same diurnal OFS trend: an early morning (8:00-12:00) VOCs-limited/transition regime shifting to a NO_X-limited regime around midday (13:00), followed by a return to VOCs-limited/transition conditions in the afternoon (14:00-18:00). This midday transition to NO_X-limited conditions is chemically reasonable, where intensified NO_2 photolysis boosts O_X production while persistent photochemistry consumption without replenishment (Wang et al., 2023). The overall OFS classification (mainly VOCs-limited and transition regimes) aligns with previous studies in Guangdong in autumn (Song et al., 2022; Chen et al., 2020b; Wu et al., 2020; Jing et al., 2024). However, the OFS assessment results from measured and modelling methods showed only 60 % agreement in hourly OFS variations (see Fig. S14).

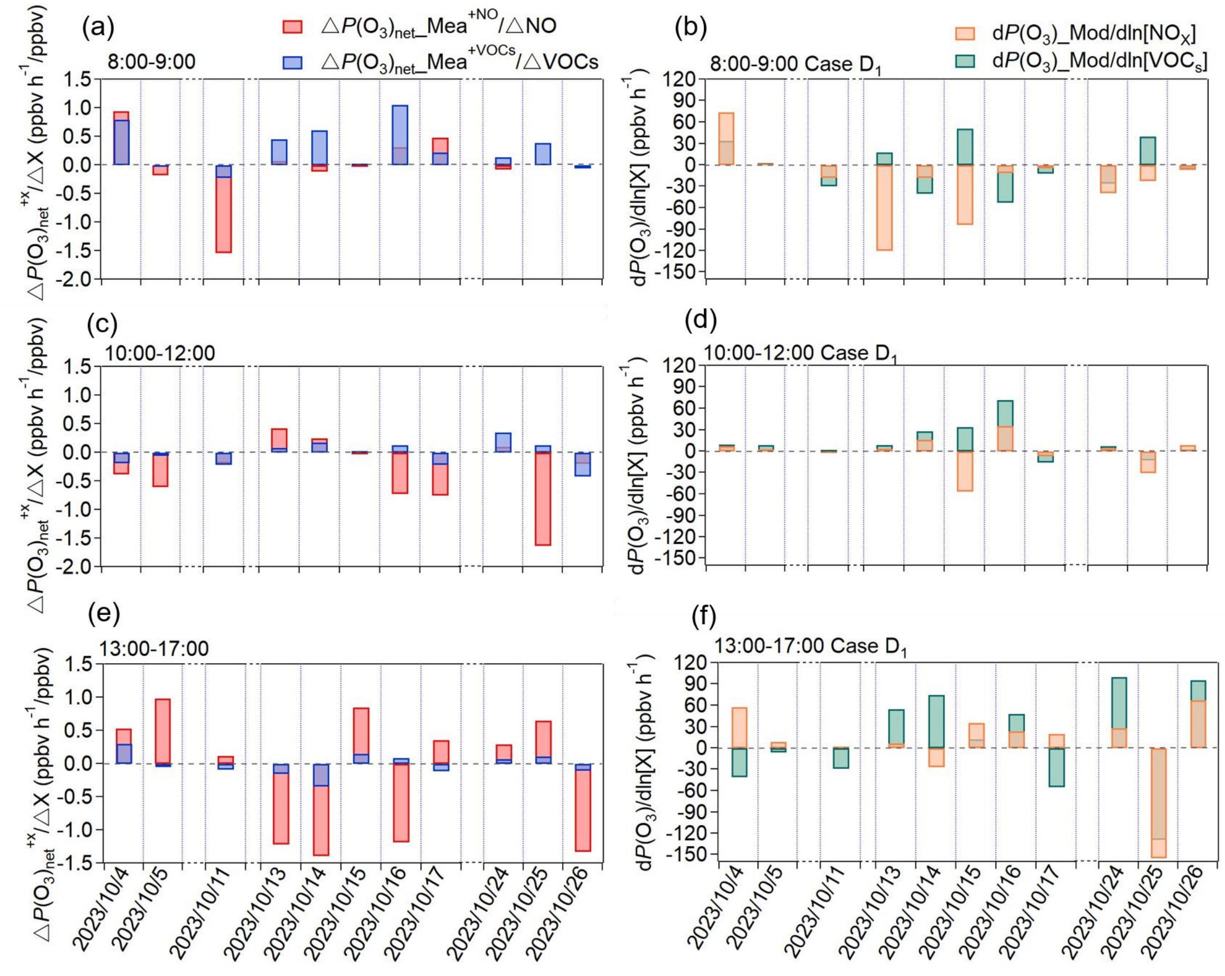

Figure 6: Average values of IR derived from the direct measurement data using the NPOPR detection system (e.g., $\Delta P(O_3)_{net}^{+NO}$ and $\Delta P(O_3)_{net}^{+VOCs}$) and absolute $P(O_3)_{net}$ sensitivity from the box model during (a)–(b) $P(O_3)_{net}$ rising phase (8:00-9:00) ; (c)–(d) $P(O_3)_{net}$ stable phase (10:00-12:00) (e)–(f) $P(O_3)_{net}$ declining phase (13:00-17:00).

In order to gain a deeper understanding of the similarities and differences between the direct measurement and the model simulation methods in diagnosing OFS, we divided the daytime observation period into three characteristic phases: the $P(O_3)_{net}$

rising phase (8:00-9:00), the $P(O_3)_{net}$ stable phase (10:00-12:00), and the $P(O_3)_{net}$ declining phase (13:00-17:00). Fig. 6 (a), (c), and (e) present the diurnal cumulative average results of IR derived from direct measurements of $\Delta P(O_3)_{net}^{+NO}$ and $\Delta P(O_3)_{net}^{+VOCs}$ using the NPOPR detection system for each phase. Fig. 6 (b), (d), and (f) show the diurnal cumulative average results of the absolute $P(O_3)_{net}$ sensitivity calculated from the box model (Case D_1) for each phase. We found that during the $P(O_3)_{net}$ rising phase, both the direct measurement and the model simulation methods identified the OFS as being in either the transition regime or VOCs-limited regime. However, the agreement between these two methods was only 63.6 %. During the $P(O_3)_{net}$ stable phase, the consistency between these two methods improved significantly, reaching 72.7 %, with the OFS predominantly located in the transition regime. This higher consistency occurred during periods of higher solar radiation intensity, when photochemical reactions were more stable, leading to improved model simulation accuracy. During the $P(O_3)_{net}$ declining phase, the two methods achieved an agreement of 72.7 % in the OFS assessment; both predominantly identified the OFS as being in either the transition regime or NO_X-limited regime. This relatively high agreement may be attributed to the reduced intensity of solar radiation and the decreased complexity of photochemical reactions in the afternoon. As Chen et al. (2025) showed that lower solar radiation simplifies reaction pathways, thereby enhancing model simulation accuracy. To illustrate that the diurnal shift in OFS depicted in Fig. 6 is not random noise but reflects the general rule, we grouped the 11 days of direct measurements by their initial O_3-formation regime, calculated their average diurnal variations, and thus reproduced the "morning-transition" phenomenon in Fig. S13c–d.

The absolute $P(O_3)_{net}$ sensitivity for scenarios Case E_1–Case E_3 are shown in Fig. S15. The agreement between these scenarios and the direct measurement results changes across different periods, with consistency levels of 54.5–63.6 %, 45.5–72.7 %, and 63.6–72.7 % during $P(O_3)_{net}$ rising phase, $P(O_3)_{net}$ stable phase, and $P(O_3)_{net}$ declining phase, respectively. In cases where $P(O_3)_{net_}$Missing was reduced (Case E_1–Case E_3), the OFS sometimes shifted to NO_X-limited conditions during certain periods, such as in Case E_2 during the $P(O_3)_{net}$ rising phase and Case E3 during the $P(O_3)_{net}$ stable phase on October 4, 2023. This contradictory phenomenon may be related to the model's incomplete representation of unknown high-reactivity VOCs chemical mechanisms (e.g., aldehyde and ketone). Additionally, previous studies have pointed out that the diagnostic method based on the box model tends to overestimate the sensitivity to VOCs in certain regions of China due to neglecting the reactivity of unidentified VOCs in anthropogenic emissions (Xu et al., 2022; Lu et al., 2010). To more accurately simulate O_3 formation and precursor sensitivity, Xu et al. (2022) incorporated formaldehyde as input data in the box model, and found that this improvement significantly reduced the model's bias in diagnosing OFS, particularly in misjudging the VOCs-limited regime. These results demonstrate that the bias between measured and modeled OFS arises chiefly from missing VOCs or shortcomings in the model's chemical mechanism.

It is noteworthy that there are differences in the precursor sensitivity response mechanisms between the absolute $P(O_3)_{net}$ sensitivity assessment method based on the box model and the IR method based on the direct measurement method. For example, during the $P(O_3)_{net}$ stable phase (10:00-12:00 period) on 4–5 October, although both methods identified the OFS as being in the transition regime, the direct measurement showed that an increase in precursor concentrations suppressed $P(O_3)_{net}$, while the model simulations indicated that a reduction in precursor concentrations led to a decrease in $P(O_3)_{net}$. However, these findings only explain regional differences in sensitivity determinations, and the underlying reasons for the differing precursor sensitivity response mechanisms between the two methods may require further investigation.

5 Conclusions

Understanding ozone (O_3) production mechanisms is critical for accurate O_3 pollution assessment and control, as photochemical production directly effects O_3 concentration levels. Due to the absence of certain mechanisms in conventional models, particularly the kinetics from missing reactive volatile organic compounds (VOCs) species, the reliability of net photochemical O_3 production rates ($P(O_3)_{net}$) and O_3 formation sensitivity (OFS) evaluation is compromised. To address this issue, we employed the custom-made online O_3 production rate (NPOPR) detection system based on the dual-reaction chamber technique to measure the $P(O_3)_{ne}$ and OFS. The system was applied in field observations at the Guangdong Atmospheric Supersite of China in Heshan, Pearl River Delta during the autumn of 2023. By combining the NPOPR detection system and the box model, a systematic investigation of $P(O_3)_{net}$ and OFS was carried out. During the observation period (4–26 October 2023), a total of 6 O_3 pollution days were recorded, with the maximum O_3 mixing ratio reaching 136.5 ppbv. The $P(O_3)_{net}$ levels on O_3 pollution days were significantly higher than those on normal days, indicating that high temperatures, low humidity, strong solar radiation, and stagnant weather conditions favor the O_3 pollution formation. The observational results show that oxygenated volatile organic compounds (OVOCs) and aromatic hydrocarbons contributing 51.6 % and 32.9 % to OFP, respectively, which are the primary contributors to O_3 formation.

Systematic underestimation of modelled $P(O_3)_{net}$ ($P(O_3)_{net_}$Mod) was found when compared to the measured $P(O_3)_{net}$ ($P(O_3)_{net_}$Mea); this difference is defined as upper-limit $P(O_3)_{net_}$Missing due to the overestimation of HONO by MARGA in this study. When gradually incorporating mechanisms such as HO_2 uptake by ambient aerosols, dry deposition, N_2O_5 uptake, and $ClNO_2$ photolysis (Case D_1), the daytime average $P(O_3)_{net_}$Missing was 3.4 ppbv h^{-1} (26.3 % underestimation). After adding constraints for VOC species such as acetaldehyde, acrolein, acetone, and butanone compared to Case D_1 (defined as Case D_2), the $P(O_3)_{net_}$Mod decreased by 0.5 % compared with Case D_1. However, after further constraining all measurable OVOC species (Case D_3), $P(O_3)_{net_}$Mod values increased by 4.4 % compared with Case D_2, with a notable improvement of 10.2 % (approximately 1.3 ppbv h^{-1}) during the $P(O_3)_{net}$ rising phase (8:00-9:00). This indicates that OVOCs play a particularly significant role in O_3 formation during the morning. Additionally, after adding chlorine-containing VOCs (Case D_4), $P(O_3)_{net_}$Mod increased by only 1.1 % compared with Case D_3, further confirming the dominant role of OVOCs in compensating for $P(O_3)_{net_}$Missing. These results also demonstrate that incorporating the aforementioned missing mechanisms and measured VOC species cannot fully eliminate simulation bias. Other processes, i.e., the RO_2, autoxidation, and the accretion reactions can also affect modelled $P(O_3)_{net}$, but they have not been examined here. The negative correlation of $P(O_3)_{net_}$Missing with the air mass aging indicates that the $P(O_3)_{net}$ missing is not likely caused by unaccounted secondary production.

To quantify the effect of unmeasured VOCs and their related reactions, especially those involving OVOCs, we developed a compensation approach based on the observed relationship between daytime averaged $P(O_3)_{net_}$Missing and $k_{OH\_}$ Missing.

This approach hypothesizes that upscaling measured VOCs can compensate for the $k_{OH\_}$ Missing attributed to unmeasured species, thereby reducing $P(O_3)_{net_}$Missing. Building upon Case D_1, we designed three modelling scenarios (Case E_1: expanded TVOC; Case E_2: expanded ethylene and formaldehyde; Case E_3: expanded formaldehyde) to compensate for $P(O_3)_{net_}$Missing. Among these modelling scenarios, the daytime averaged $P(O_3)_{net_}$Missing was reduced to 10.3 %, 17.2 %, and 5.1 % for Case E_1, Case E_2, and Case E_3, respectively. Notably, Case E_3 achieved the greatest reduction solely by increasing formaldehyde concentrations, validating the critical role of highly reactive OVOCs (particularly formaldehyde) in compensating for $P(O_3)_{net_}$Missing. This suggests that there other unmeasured highly reactive VOC species may exist in the ambient atmosphere, and constraining them in the model could further improve the simulation accuracy.

Additionally, the sensitivity assessment results derived from the different measured and modelled OFS approaches were compared: (1) in direct measurement using the NPOPR detection system, NO or VOCs were added to quantify changes in $P(O_3)_{net}$, with OFS determined through the incremental reactivity (IR) index (IR=$\Delta P(O_3)_{net}^{+x}/\Delta S(x)$, where X = NOx or VOCs and ΔS(x) represents the added concentration); (2)in model simulations, where the box model calculated $P(O_3)_{net}$ and derived absolute $P(O_3)_{net}$ sensitivity ($dP(O_3)_{net}/d[X]$, where X = NOx or VOCs). Meanwhile we found that the agreement of OFS assessment results between the direct measurements and the model results was lower in the $P(O_3)_{net}$ rising phase (8:00-9:00, 63.6 %) than those in the $P(O_3)_{net}$ stable phase (10:00-12:00, 72.7 %) and $P(O_3)_{net}$ declining phase (13:00-17:00, 72.7 %). This again highlights the importance of highly reactive OVOCs in improving the accuracy of OFS assessment. These results indicate that reducing $P(O_3)_{net_}$Missing can enhance the accuracy of OFS assessment to some extent, but fully eliminating the discrepancies still requires further constraints on unmeasured VOC species and further research.

In conclusion, we quantitatively assessed the $P(O_3)_{net}$ simulation deficits and their impact on OFS diagnosis by comparing the measured and modelled $P(O_3)_{net}$, and found that the unmeasured VOCs —rather than the secondary atmospheric formation —are the primary causative factor of $P(O_3)_{net_}$Missing. Furthermore, both direct measurements and model results reveal a diurnal OFS shift dominated by the morning regime; transition and VOC-limited conditions prevailed, so prioritizing VOCs while co-controlling NO_X is the most effective approach to O_3 pollution control in PRD region. Our results also demonstrate that the persistent model biases risk under-estimating the local photochemical formation contribution to O_3 pollution, thereby has weakening its perceived impact relative to physical transportation. Future studies should expanded VOCs measurements and combine direct $P(O_3)_{net}$ observations with regional transport model to separate local production from up-wind advection.

Date availability. The datasets supporting this research are included in this manuscript and its supplementary information files. The data for this study are also publicly available at https://doi.org/10.5281/zenodo.15052519. Meteorological data were sourced from the European Centre for Medium-Range Weather Forecasts (ECMWF, https://www.ecmwf.int/). Box model simulations were conducted using the AtChem2 model (https://atchem.leeds.ac.uk/webapp/) with the Master Chemical Mechanism (MCM v3.3.1, https://mcm.york.ac.uk/MCM). Figures in this study were created using Igor Pro 6.7. Additional data or materials related to this study can be made available upon reasonable request to the corresponding author (junzhou@jnu.edu.cn), subject to restrictions on data resources.

Supplement. The supplement related to this article is available online at: https://doi.org/

Author contributions. Author contributions. JZ and MS designed this study. JZ and BZ wrote the manuscript with contributions from all co-authors. JZ, BJ, BZ, TZ, DC, YZ, J. Li, MD, MX, JHJ, and J. Luo collected and analyzed the data. All authors reviewed and revised the manuscript.

Competing interests. The contact author has declared that none of the authors has any competing interests.

Acknowledgments. Many thanks to the Guangdong Ecological and Environmental Monitoring Center.

Financial support. This work was funded by the National Natural Science Foundation of China (No. 42305096), the Special Support Plan for High-Level Talents of Guangdong Province (No. 2023JC07L057), the Natural Science Foundation of Guangdong Province (No. 2024A1515011494), the National Key Research and Development Program of China (No. 2023YFC3706204), and the Guangdong Provincial Basic and Applied Basic Research Fund (the Youth Doctoral "Launch" Project) for the Year 2025 (No. SL2024A04J00396). Jianhui Jiang was supported by the National Natural Science Foundation of China (No. 42207122).

References

Baier, B. C., Brune, W. H., Lefer, B. L., Miller, D. O., and Martins, D. K.: Direct ozone production rate measurements and their use in assessing ozone source and receptor regions for Houston in 2013, Atmospheric Environment, 114, 83-91, doi: 10.1016/j.atmosenv.2015.05.033, 2015.

Baier, B. C., Brune, W. H., Miller, D. O., Blake, D., Long, R., Wisthaler, A., Cantrell, C., Fried, A., Heikes, B., and Brown, S.: Higher measured than modeled ozone production at increased NO_X levels in the Colorado Front

Berndt, T., Mentler, B., Scholz, W., Fischer, L., Herrmann, H., Kulmala, M., Hansel A.: 2018. Accretion product formation from Ozonolysis and OH radical reaction of α-Pinene: mechanistic insight and the influence of isoprene and ethylene, Environmental Science & Technology, 52, 11069–11077, doi: 10.1021/acs.est.8b02210, 2018.

Cai, C., Geng, F., Tie, X., Yu, Q., and An, J.: Characteristics and source apportionment of VOCs measured in Shanghai, China, Atmospheric Environment, 44, 5005-5014, doi: 10.1016/j.atmosenv.2010.07.059, 2010.

Cazorla, M. and Brune, W.: Measurement of ozone production sensor, Atmospheric Measurement Techniques Discussions, 2, 3339-3368, doi: 10.5194/amtd-2-3339-2009, 2009.

Carter, W. P. L., A. Pierce J. A., Luo, D., Malkina, I. L.: Environmental chamber study of maximum incremental reactivities of volatile organic-compounds, Atmospheric Environment, 29, 2499, doi.org/10.1016/1352-2310(95)00149-S, 1995.

Cazorla, M., Brune, W., Ren, X., and Lefer, B.: Direct measurement of ozone production rates in Houston in 2009 and comparison with two estimation methods, Atmospheric Chemistry and Physics, 12, 1203-1212, doi: 10.5194/acp-12-1203-2012, 2012.

Chen, L., Liao, H., Zhu, J., Li, K., Bai, Y., Yue, X., Yang, Y., Hu, J., and Zhang, M.: Increases in ozone-related mortality in China over 2013–2030 attributed to historical ozone deterioration and future population aging, Science of The Total Environment, 858, 159972, doi: 10.1016/j.scitotenv.2022.159972, 2023.

Chen, S., Wei, W., Wang, C., Wang, X., Zhou, C., and Cheng, S.: A modeling approach to dynamically estimating local photochemistry process and its contribution to surface O3 pollution, Journal of Environmental Management, 373, 123450, doi: 10.1016/j.jenvman.2024.123450, 2025.

Chen, T., Xue, L., Zheng, P., Zhang, Y., Liu, Y., Sun, J., Han, G., Li, H., Zhang, X., and Li, Y.: Volatile organic compounds and ozone air pollution in an oil production region in northern China, Atmospheric Chemistry and Physics, 20, 7069-7086, doi: 10.5194/acp-20-7069-2020, 2020a.

Chen, Y., Chi, S., Wang, Y., Guo, S., Zhang, C., Ye, C., and Lin, W.: Ozone production sensitivity in the highland city of Lhasa: a comparative analysis with Beijing, Air Quality, Atmosphere & Health, 1-11, doi: 10.1007/s11869-024-01604-4, 2024.

Chen, Y., Yan, H., Yao, Y., Zeng, C., Gao, P., Zhuang, L., Fan, L., and Ye, D.: Relationships of ozone formation sensitivity with precursors emissions, meteorology and land use types, in Guangdong-Hong Kong-Macao Greater Bay Area, China, Journal of Environmental Sciences, 94, 1-13, doi: 10.1016/j.jes.2020.04.005, 2020b.

Crounse, J. D., Knap, H. C., Ørnsø, K. B., Jørgensen, S., Paulot, F, Kjaergaard, H. G., and Wennberg, P. O.: Atmospheric Fate of Methacrolein. 1. Peroxy Radical Isomerization Following Addition of OH and O_2. The Journal of Physical Chemistry A, 116, 5756-5762, doi.org/10.1021/jp211560u, 2012.

Dyson, J. E., Whalley, L. K., Slater, E. J., Woodward-Massey, R., Ye, C., Lee, J. D., Squires, F., Hopkins, J. R., Dunmore, R. E., and Shaw, M.: Impact of HO_2 aerosol uptake on radical levels and O_3 production during summertime in Beijing, Atmospheric Chemistry and Physics Discussions, 2022, 1-43, doi: 10.5194/acp-2022-800, 2022.

de Gouw, J., Middlebrook, A., Warneke, C., Goldan, P., Kuster, W., Roberts, J., Fehsenfeld, F., Worsnop, D., Canagaratna, M., and Pszenny, A.: Budget of organic carbon in a polluted atmosphere: Results from the New England Air Quality Study in 2002, Journal of Geophysical Research-Atmospheres, 110, D16305, doi.org/10.1029/2004JD005623, 2005.

Gilman, J. B., Kuster, W. C., Goldan, P. D., Herndon, S. C., Zahniser, M. S., Tucker, S. C., Brewer, W. A., Lerner, B. M., Williams, E. J., and Harley, R. A.: Measurements of volatile organic compounds during the 2006 TexAQS/GoMACCS campaign: Industrial influences, regional characteristics, and diurnal dependencies of the OH reactivity, Journal of Geophysical Research: Atmospheres, 114, doi: 10.1029/2008jd011525, 2009.

Yu, G., Lin L., Xia S., Zhu B., and Huang X.: The characteristics of VOCs and ozone formation sensitivity in a typical industrial area in Shenzhen, China Environmental Science, 42, 1994-2001, doi: 10.19674/j.cnki.issn1000-6923.20220112.015, 2022.

Hao, Y., Zhou, J., Zhou, J.-P., Wang, Y., Yang, S., Huangfu, Y., Li, X.-B., Zhang, C., Liu, A., and Wu, Y.: Measuring and modeling investigation of the net photochemical ozone production rate via an improved dual-channel reaction chamber technique, Atmospheric Chemistry and Physics, 23, 9891-9910, doi: 10.5194/acp-23-9891-2023, 2023.

Jeffries, H.: An experimental method for measuring the rate of synthesis, destruction, and transport of ozone in the lower atmosphere, Ph. D. Thesis, Department of Environmental Science and Engineering, 1971.

Jing, S., Duohong, C., Wang, C., Ridong, C., Yu-jun, L., Yongxi, H., Xin, Z., and Yan, Z.: Study on the Characteristics and Causes of Ozone Severe Pollution Days in Jiangmen City, China Environmental Science, 1-19, doi: 10.19674/j.cnki.issn1000-6923.20241212.002, 2024.

Kanaya, Y., Hofzumahaus, A., Dorn, H.-P., Brauers, T., Fuchs, H., Holland, F., Rohrer, F., Bohn, B., Tillmann, R., and Wegener, R.: Comparisons of observed and modeled OH and HO_2 concentrations during the ambient measurement period of the HO_X Comp field campaign, Atmospheric Chemistry and Physics, 12, 2567-2585, doi: 10.5194/acp-12-2567-2012, 2012.

Li, B., Gasser, T., Ciais, P., Piao, S., Tao, S., Balkanski, Y., Hauglustaine, D., Boisier, J.-P., Chen, Z., and Huang, M.: The contribution of China's emissions to global climate forcing, Nature, 531, 357-361, doi: 10.1038/nature17165, 2016.

Li, K., Jacob, D. J., Liao, H., Shen, L., Zhang, Q., and Bates, K. H.: Anthropogenic drivers of 2013–2017 trends in summer surface ozone in China, Proceedings of the National Academy of Sciences, 116, 422-427, doi: 10.1073/pnas.1812168116, 2019.

Li, K., Wang, X., Li, L., Wang, J., Liu, Y., Cheng, X., Xu, B., Wang, X., Yan, P., and Li, S.: Large variability of O_3-precursor relationship during severe ozone polluted period in an industry-driven cluster city (Zibo) of North China Plain, Journal of Cleaner Production, 316, 128252, doi: 10.1016/j.jclepro.2021.128252, 2021.

Lu, K., Zhang, Y., Su, H., Brauers, T., Chou, C. C., Hofzumahaus, A., Liu, S. C., Kita, K., Kondo, Y., and Shao, M.: Oxidant (O_3+ NO_2) production processes and formation regimes in Beijing, Journal of Geophysical Research: Atmospheres, 115, doi: 10.1029/2009JD012714, 2010.

Lyu, Y., Gao, Y., Pang, X., Sun, S., Luo, P., Cai, D., Qin, K., Wu, Z., and Wang, B.: Elucidating contributions of volatile organic compounds to ozone formation using random forest during COVID-19 pandemic: A case study in China, Environmental Pollution, 346, 123532, doi: 10.1016/j.envpol.2024.123532, 2024.

Ma, W., Chen, X., Xia, M., Liu, Y., Wang, Y., Zhang, Y., Zheng, F., Zhan, J., Hua, C., and Wang, Z.: Reactive Chlorine Species Advancing the Atmospheric Oxidation Capacities of Inland Urban Environments, Environmental Science & Technology, 57, 14638-14647, doi: 10.1021/acs.est.3c05169, 2023.

Ma, W., Feng, Z., Zhan, J., Liu, Y., Liu, P., Liu, C., Ma, Q., Yang, K., Wang, Y., and He, H.: Influence of photochemical loss of volatile organic compounds on understanding ozone formation mechanism, Atmospheric Chemistry and Physics, 22, 4841-4851, doi: 10.5194/acp-22-4841-2022, 2022.

Mazaheri, M., Lin, W., Clifford, S., Yue, D., Zhai, Y., Xu, M., Rizza, V., and Morawska, L.: Characteristics of school children's personal exposure to ultrafine particles in Heshan, Pearl River Delta, China–A pilot study, Environment International, 132, 105134, doi: 10.1016/j.envint.2019.105134, 2019.

Morino, Y., Sadanaga, Y., Sato, K., Sakamoto, Y., Muraoka, T., Miyatake, K., Li, J., and Kajii, Y.: Direct evaluation of the ozone production regime in smog chamber experiments, Atmospheric Environment, 309, 119889, doi: 10.1016/j.atmosenv.2023.119889, 2023.

Mousavinezhad, S., Choi, Y., Pouyaei, A., Ghahremanloo, M., and Nelson, D. L.: A comprehensive investigation of surface ozone pollution in China, 2015–2019: Separating the contributions from meteorology and precursor emissio ns, Atmospheric Research, 257, 105599, doi: 10.1016/j.atmosres.2021.105599, 2021.

Qian, H., Xu, B., Xu, Z., Zou, Q., Zi, Q., Zuo, H., Zhang, F., Wei, J., Pei, X., and Zhou, W.: Anthropogenic Oxygenated Volatile Organic Compounds Dominate Atmospheric Oxidation Capacity and Ozone Production via Secondary Formation of Formaldehyde in the Urban Atmosphere, ACS ES&T Air, doi.org/10.1021/acsestair.4c00317, 2025.

Pei, C. L., Xie, Y. T., Chen, X., Zhang, T., Qiu, X. N., Wang, Y., Wang, Z. H., and Li, M.: Analysis of a Typical Ozone Pollution Process in Guangzhou in Winter, Environmental Science, 43, 4305-4315, doi: 10.13227/j.hjkx.202110168, 2022.

Ren, X., Van Duin, D., Cazorla, M., Chen, S., Mao, J., Zhang, L., Brune, W. H., Flynn, J. H., Grossberg, N., and Lefer, B. L.: Atmospheric oxidation chemistry and ozone production: Results from SHARP 2009 in Houston, Texas, Journal of Geophysical Research: Atmospheres, 118, 5770-5780, doi: 10.1002/jgrd.50342, 2013.

Sadanaga, Y., Kawasaki, S., Tanaka, Y., Kajii, Y., and Bandow, H.: New system for measuring the photochemical ozone production rate in the atmosphere, Environmental science & technology, 51, 2871-2878, doi: 10.1021/acs.est.6b04639, 2017.

Sakamoto, Y., Sadanaga, Y., Li, J., Matsuoka, K., Takemura, M., Fujii, T., Nakagawa, M., Kohno, N., Nakashima, Y., and Sato, K.: Relative and absolute sensitivity analysis on ozone production in Tsukuba, a city in Japan, Environmental science & technology, 53, 13629-13635, doi: 10.1021/acs.est.9b03542, 2019.

Seinfeld, J. H. and Pandis, S. N. (Eds. 3): Atmospheric Chemistry and Physics: From Air Pollution to Climate Change, John Wiley & Sons, Hoboken, ISBN 978-1-118-94740-1, 2016.

Sillman, S.: The relation between ozone, NOx and hydrocarbons in urban and polluted rural environments, Atmospheric Environment, 33, 1821–1845, https://doi.org/10.1016/S1352-2310(98)00345-8, 1999.

Sklaveniti, S., Locoge, N., Stevens, P. S., Wood, E., Kundu, S., and Dusanter, S.: Development of an instrument for direct ozone production rate measurements: Measurement reliability and current limitations, Atmospheric Measurement Techniques, 11, 741-761, doi: 10.1029/98jd00349, 2018.

Sommariva, R., Cox, S., Martin, C., Borońska, K., Young, J., Jimack, P. K., Pilling, M. J., Matthaios, V. N., Nelson, B. S., and Newland, M. J.: AtChem (version 1), an open-source box model for the Master Chemical Mechanism, Geoscientific Model Development, 13, 169-183, doi: 10.5194/gmd-13-169-2020, 2020.

Song, K., Liu, R., Wang, Y., Liu, T., Wei, L., Wu, Y., Zheng, J., Wang, B., and Liu, S. C.: Observation-based analysis of ozone production sensitivity for two persistent ozone episodes in Guangdong, China, Atmospheric Chemistry and Physics, 22, 8403-8416, doi: 10.5194/acp-22-8403-2022, 2022.

Tan, Z., Fuchs, H., Lu, K., Hofzumahaus, A., Bohn, B., Broch, S., Dong, H., Gomm, S., Häseler, R., and He, L.: Radical chemistry at a rural site (Wangdu) in the North China Plain: observation and model calculations of OH, HO_2 and RO_2 radicals, Atmospheric Chemistry and Physics, 17, 663-690, doi: 10.5194/acp-17-663-2017, 2017.

Tan, Z., Lu, K., Dong, H., Hu, M., Li, X., Liu, Y., Lu, S., Shao, M., Su, R., and Wang, H.: Explicit diagnosis of the local ozone production rate and the ozone-NOx-VOC sensitivities, Science bulletin, 63, 1067-1076, doi: 10.1016/j.scib.2018.07.001, 2018.

Tan, Z., Lu, K., Hofzumahaus, A., Fuchs, H., Bohn, B., Holland, F., Liu, Y., Rohrer, F., Shao, M., and Sun, K.: Experimental budgets of OH, HO_2, and RO_2 radicals and implications for ozone formation in the Pearl River Delta in China 2014, Atmospheric chemistry and physics, 19, 7129-7150, doi: 10.5194/acp-2018-801, 2019.

Tong, J., Hu, R., Hu, C., Liu, X., Cai, H., Lin, C., Zhong, L., Wang, J., and Xie, P.: Development of a net ozone production rate detection system based on dual-channel cavity ring-down spectroscopy, Journal of Environmental Sciences, 149, 419-430, doi: 10.1016/j.jes.2024.01.035, 2025.

Wang, J., Zhang, Y., Wu, Z., Luo, S., Song, W., and Wang, X.: Ozone episodes during and after the 2018 Chinese National Day holidays in Guangzhou: Implications for the control of precursor VOCs, Journal of Environmental Sciences, 114, 322-333, doi: 10.1016/j.jes.2021.09.009, 2022a.

Wang, P., Chen, Y., Hu, J., Zhang, H., and Ying, Q.: Attribution of tropospheric ozone to NOx and VOC emissions: considering ozone formation in the transition regime, Environmental Science & Technology, 53, 1404–1412, https://doi.org/10.1021/acs.est.8b05981, 2019.

Wang, R., Wang, L., Sun, J., Zhang, L., Li, Y., Li, K., Liu, B., Zhang, J., and Wang, Y.: Maximizing ozone control by spatial sensitivity-oriented mitigation strategy in the Pearl River Delta Region, China, Science of The Total Environment, 905, 166987, doi: 10.1016/j.scitotenv.2023.166987, 2023.

Wang, S, Wu, R, Berndt, T, Ehn, M, Wang, L.: Formation of highly oxidized radicals and multifunctional products from the atmospheric oxidation of Alkylbenzenes, Environmental Science & Technology, 51, 8442-8449, DOI: 10.1021/acs.est.7b02374, 2017.

Wang, T., Xue, L., Brimblecombe, P., Lam, Y. F., Li, L., and Zhang, L.: Ozone pollution in China: A review of concentrations, meteorological influences, chemical precursors, and effects, Science of the Total Environment, 575, 1582-1596, doi: 10.1016/j.scitotenv.2016.10.081, 2017.

Wang, W., Li, X., Cheng, Y., Parrish, D. D., Ni, R., Tan, Z., Liu, Y., Lu, S., Wu, Y., and Chen, S.: Ozone pollution mitigation strategy informed by long-term trends of atmospheric oxidation capacity, Nature Geoscience, 17, 20-25, doi: 10.1038/s41561-023-01334-9, 2024a.

Wang, W., Yuan, B., Peng, Y., Su, H., Cheng, Y., Yang, S., Wu, C., Qi, J., Bao, F., and Huangfu, Y.: Direct observations indicate photodegradable oxygenated volatile organic compounds (OVOCs) as larger contributors to radicals and ozone production in the atmosphere, Atmospheric Chemistry and Physics, 22, 4117-4128, doi: 10.5194/acp-22-4117-2022, 2022b.

Wang, W., Yuan, B., Su, H., Cheng, Y., Qi, J., Wang, S., Song, W., Wang, X., Xue, C., and Ma, C.: A large role of missing volatile organic compound reactivity from anthropogenic emissions in ozone pollution regulation, Atmospheric Chemistry and Physics, 24, 4017-4027, doi: 10.5194/acp-24-4017-2024, 2024b.

Wang, Y., Chen, Y., Chi, S., Wang, J., Zhang, C., Lin, W., Zhao, W., and Ye, C.: Optimizing a twin-chamber system for direct ozone production rate measurement, Environmental Pollution, 348, 123837, doi: 10.1016/j.envpol.2024.123837, 2024.

Wei, N., Zhao, W., Yao, Y., Wang, H., Liu, Z., Xu, X., Rahman, M., Zhang, C., Fittschen, C., and Zhang, W.: Peroxy radical chemistry during ozone photochemical pollution season at a suburban site in the boundary of Jiangsu–Anhui–Shandong–Henan region, China, Science of the Total Environment, 904, 166355, doi: 10.1016/j.scitotenv.2023.166355, 2023.

Whalley, L. K., Slater, E. J., Woodward-Massey, R., Ye, C., Lee, J. D., Squires, F., Hopkins, J. R., Dunmore, R. E., Shaw, M., and Hamilton, J. F.: Evaluating the sensitivity of radical chemistry and ozone formation to ambient VOCs and NO_X in Beijing, Atmospheric Chemistry and Physics, 21, 2125-2147, doi: 10.5194/acp-2020-785, 2021.

Woodward-Massey, R., Sommariva, R., Whalley, L. K., Cryer, D. R., Ingham, T., Bloss, W. J., Ball, S. M., Cox, S., Lee, J. D., and Reed, C. P.: Radical chemistry and ozone production at a UK coastal receptor site, Atmospheric Chemistry and Physics, 23, 14393-14424, doi: 10.5194/acp-23-14393-2023, 2023.

Wu, C., Wang, C., Wang, S., Wang, W., Yuan, B., Qi, J., Wang, B., Wang, H., Wang, C., Song, W., Wang, X., Hu, W., Lou, S., Ye, C., Peng, Y., Wang, Z., Huangfu, Y., Xie, Y., Zhu, M., Zheng, J., Wang, X., Jiang, B., Zhang, Z., and Shao, M.: Measurement report: Important contributions of oxygenated compounds to emissions and chemistry of volatile organic compounds in urban air, Atmospheric Chemistry and Physics, 20, 14769-14785, doi: 10.5194/acp-20-14769-2020, 2020.

Wu, S., Lee, H. J., Anderson, A., Liu, S., Kuwayama, T., Seinfeld, J. H., and Kleeman, M. J.: Direct measurements of ozone response to emissions perturbations in California, Atmospheric Chemistry and Physics, 22, 4929-4949, oi.org/10.5194/acp-22-4929-2022, 2022.

Xu, D., Yuan, Z., Wang, M., Zhao, K., Liu, X., Duan, Y., Fu, Q., Wang, Q., Jing, S., and Wang, H.: Multi-factor reconciliation of discrepancies in ozone-precursor sensitivity retrieved from observation-and emission-based models, Environment International, 158, 106952, doi: 10.1016/j.envint.2021.106952, 2022.

Yadav, P., Lal, S., Tripathi, S. N., Jain, V., and Mandal, T. K.: Role of sources of NMVOCs in O_3, OH reactivity, and secondary organic aerosol formation over Delhi, Atmospheric Pollution Research, 15, 102082, doi: 10.1016/j.apr.2024.102082, 2024.

Yang, M., Li, F., Huang, C., Tong, L., Dai, X., and Xiao, H.: VOC characteristics and their source apportionment in a coastal industrial area in the Yangtze River Delta, China, Journal of Environmental Sciences, 127, 483-494, doi: 10.1016/j.jes.2022.05.041, 2023.

Yang, X., Lu, K., Ma, X., Gao, Y., Tan, Z., Wang, H., Chen, X., Li, X., Huang, X., and He, L.: Radical chemistry in the Pearl River Delta: observations and modeling of OH and HO_2 radicals in Shenzhen 2018, Atmospheric Chemistry and Physics Discussions, 2022, 1-19, doi: 10.5194/acp-22-12525-2022, 2022.

Yang, Y., Shao, M., Keßel, S., Li, Y., Lu, K., Lu, S., Williams, J., Zhang, Y., Zeng, L., and Nölscher, A. C.: How the OH reactivity affects the ozone production efficiency: case studies in Beijing and Heshan, China, Atmospheric Chemistry and Physics, 17, 7127-7142, doi: 10.5194/acp-17-7127-2017, 2017.

Yu, D., Tan, Z., Lu, K., Ma, X., Li, X., Chen, S., Zhu, B., Lin, L., Li, Y., and Qiu, P.: An explicit study of local ozone budget and NOx-VOCs sensitivity in Shenzhen China, Atmospheric Environment, 224, 117304, doi: 10.1016/j.atmosenv.2020.117304, 2020.

Yuan, B., Shao, M., De Gouw, J., Parrish, D. D., Lu, S., Wang, M., Zeng, L., Zhang, Q., Song, Y., and Zhang, J.: Volatile organic compounds (VOCs) in urban air: How chemistry affects the interpretation of positive matrix factorization (PMF) analysis, Journal of Geophysical Research: Atmospheres, 117, doi.org/10.1029/2012jd018236, 2012.

Yuan, B., Hu, W. W., Shao, M., Wang, M., Chen, W. T., Lu, S. H., Zeng, L. M., and Hu, M.: VOC emissions, evolutions and contributions to SOA formation at a receptor site in eastern China, Atmospheric Chemistry and Physics, 13, 8815–8832, https://doi.org/10.5194/acp-13-8815-2013, 2013.

Zhang, G., Yu, X., Yin, H., Feng, C., Ma, C., Sun, S., Cheng, H., Wang, S., Shang, K., and Liu, X.: Heatwave-amplified atmospheric oxidation in a multi-province border area in Xuzhou, China, Frontiers in Environmental Science, 12, 1496584, doi: 10.3389/fenvs.2024.1496584, 2024.

Zhang, L., Brook, J. R., and Vet, R.: A revised parameterization for gaseous dry deposition in air-quality models, Atmospheric Chemistry and Physics, 3, 2067-2082, doi: 10.5194/acp-3-2067-2003, 2003.

Zhang, Y., Xue, L., Chen, T., Shen, H., Li, H., and Wang, W.: Development history of Observation-Based Model (OBM) and its application and prospect in atmospheric chemistry studies in China, Res. Environ. Sci, 35, 621-632, doi: 10.13198/j.issn.1001-6929.2022.01.05, 2022.

Zheng, S., Xu, X., Zhang, Y., Wang, L., Yang, Y., Jin, S., and Yang, X.: Characteristics and sources of VOCs in urban and suburban environments in Shanghai, China, during the 2016 G20 summit, Atmospheric Pollution Research, 10, 1766-1779, doi: 10.1016/j.apr.2019.07.008, 2019.

Zhou, J., Sato, K., Bai, Y., Fukusaki, Y., Kousa, Y., Ramasamy, S., Takami, A., Yoshino, A., Nakayama, T., and Sadanaga, Y.: Kinetics and impacting factors of HO_2 uptake onto submicron atmospheric aerosols during the 2019 Air QUAlity Study (AQUAS) in Yokohama, Japan, Atmospheric Chemistry and Physics, 21, 12243-12260, doi: 10.5194/acp-21-12243-2021, 2021.

Zhou, J., Wang, W., Wang, Y., Zhou, Z., Lv, X., Zhong, M., Zhong, B., Deng, M., Jiang, B., and Luo, J.: Intercomparison of measured and modelled photochemical ozone production rates: Suggestion of chemistry hypothesis regarding unmeasured VOCs, Science of The Total Environment, 951, 175290, doi: 10.1016/j.scitotenv.2024.175290, 2024a.

Zhou, J., Zhang, C., Liu, A., Yuan, B., Wang, Y., Wang, W., Zhou, J.-P., Hao, Y., Li, X.-B., and He, X.: Measurement report: Vertical and temporal variability in the near-surface ozone production rate and sensitivity in an urban area in the Pearl River Delta region, China, Atmospheric Chemistry and Physics, 24, 9805-9826, doi: 10.5194/acp-24-9805-2024, 2024b.